Journal of Molecular Structure 1334 (2025) 141880

Contents lists available at ScienceDirect

Journal of Molecular Structure

journal homepage: www.elsevier.com/locate/molstr

Binding thermodynamics of 1,3-bis(((E-1H-pyrrol-2-yl) methylene) amino) propan-2-ol palladium(II) with HSA and its intercalative behaviour in ctDNA

Sheldon Sookai *, Ayanda Majoka, Manuel A. Fernandes, Monika Nowakowska

Molecular Sciences Institute, School of Chemistry, University of the Witwatersrand, PO WITS 2050, Johannesburg, South Africa

ARTICLE INFO

Keywords:
HSA
ctDNA
Fluorescence
Molecular dynamics
DFT

ABSTRACT

The development of novel metallodrugs needs to be investigated against several criteria: (i) whether the metallodrug remains intact and what species are present at different pH levels, (ii) the stability of the drug in serum and its components, (iii) a proposed mode of action (MOA), such as its interaction with DNA, and (iv) monitoring its binding to human serum albumin (HSA), the most abundant blood protein responsible for transporting many exogenous compounds. Here, Ni(II), Pd(II) and Pt(II) chelates of a tetradentate 1,3-bis(((E-1H-pyrrol-2-yl) methylene) amino) propan-2-ol ligand, H2 L, were intended to be assessed for their stability at varying pH's and in human serum. . However, only PdL and PtL were sufficiently stable and resisted demetallation. Thereafter, we aimed to delineate how the identity of the stable d8 metal ion impacts the compound's affinity for calf thymus DNA (ctDNA). The data acquired indicates that only PdL bound to ctDNA with a K_a 0.114 (± 0.02) × 104 M through intercalation confirmed by UV-LD spectroscopy and in silico molecular dynamic (MD) simulations. Finally, we found that PdL binds to HSA in a 2:1 ratio occupying both major drug binding sites on the protein with a K_a ~6.56 ×103 M–1 at 37 °C. The thermodynamics reflect enthalpically driven ligand uptake, hinging mainly on London dispersion forces (metal ion dependent), along with general multi-site binding (i.e., 2 PdL per HSA). Although far- and near-UV CD spectroscopy indicated that the optically inactive ligands negligibly perturb the secondary and tertiary structure of HSA, substantial induced CD (ICD) spectra were recorded for the protein-bound ligands and could be simulated by hybrid QM:MM TD-DFT methods. This study highlights a step-by-step guide in going about physical biochemistry and in silico methods to analyse novel drugs.

1. Introduction

Schiff base compounds, particularly pyrrole-imine derivatives, have attracted significant attention in pharmaceutical applications due to their pronounced cytotoxicity, inherent bioactivity and facile synthesis [1–8]. These versatile pharmacores can coordinate various transition metal ions of different oxidation states [9,10], forming stable chelate complexes [11]. Examples include structurally characterised Co(II/III) [12–15], Rh(I/III) [16–19], Ir(III) [20], Ni(II) [21–23], Pd(II) [24,25], Pt(II) [26–28], Cu(II) [29–32], Ag(I) [33] and Au(III) [34] complexes. The nature of the Schiff base and centrally incorporated metal affects the activity profile and such compounds have subsequently found use in host of biological applications [3,11,35], including anti-inflammatory [36], antibacterial [37], antifungal [38], antiviral [39], antioxidant [40], antimalarial [41], and notably DNA binding [42], antitumor [43] and anticancer agents [40,44].

The ability of d^8 Schiff base imine metal complexes to target DNA has emerged as promising potential cancer therapeutics due to their ability to target DNA. The planar geometry of these complexes facilitates intercalation into DNA, disrupting replication and transcription processes crucial for tumour growth [45]. Clinically established Pt(II) complexes, such as cisplatin, have demonstrated clinical efficacy in treating various cancers [46]. However, limitations associated with resistance and toxicity [47] have spurred research into novel d^8 Schiff base imine metal complexes. For example, Pt(II) complexes bearing pyrrole-imine Schiff base ligands have shown promise in inhibiting DNA replication and inducing apoptosis in cancer cells [48,49]. Similarly, Ni (II) [37,50] and Pd(II) [51–54] complexes featuring salicylaldimine or quinoline-imine Schiff bases have exhibited potent anticancer activity through DNA binding and modulation of cellular signaling pathways.

* Corresponding author.
E-mail address: Sheldon.Sookai@wits.ac.za (S. Sookai).

https://doi.org/10.1016/j.molstruc.2025.141880
Received 13 January 2025; Received in revised form 22 February 2025; Accepted 25 February 2025
Available online 26 February 2025

Palladium(II) complexes have emerged as promising metallodrug candidates, exhibiting structural similarities to platinum-based compounds and demonstrating encouraging *in vitro* cytotoxicity. Furthermore, these complexes have been found to possess significant biological activity, including anti-HIV, antifungal, and anti-tumour properties [6]. Notably, palladium complexes exhibit fewer side effects compared to cisplatin, making them attractive alternatives for therapeutic applications. The coordination geometry of Pd(II) chelates is consistently square planar, with the palladium centre coordinated to four ligands. Strategic modification of the coordination sphere through judicious ligand selection enables precise tuning of the complex's properties. Specifically, the incorporation of nitrogen- and sulfur-donor ligands has been shown to enhance the stability and reactivity of Pd(II) complexes [55]. The potential of Pd(II) complexes as anticancer agents has been elucidated, with certain complexes exhibiting cytotoxic effects towards cancer cells. The purported mechanism of action involves interaction of the complex with DNA, resulting in inhibition of cell growth and proliferation [56]. Additionally, Pd(II) complexes have demonstrated promise as antimicrobial agents, expanding their therapeutic potential [57].

In addition to interacting with DNA, pyrrole-based metallodrugs have exhibited an affinity for Human Serum Albumin (HSA). As the most abundant plasma transport protein [58], HSA plays a pivotal role in pharmacokinetics and pharmacodynamics, influencing the solubility, stability, and bioavailability of these metal complexes [59,60]. HSA is heart-shaped structure, comprising 585 amino acids [61], binds a broad spectrum of pharmaceutical compounds and steroids [62] at Sudlow's sites I and II (Scheme 1) [63–65]. HSA's accumulation in tumours [66], facilitated by passive targeting and albumin-binding proteins like SPARC (secreted protein acidic and rich in cysteine), enables tumour-specific uptake [67]. The use of HSA as a metallodrug carrier is therefore gaining attention, leveraging its biocompatibility, biodegradability, non-immunogenicity, long circulation time, and physical stability [68,69]. Approved formulations like Abraxane [70] demonstrate

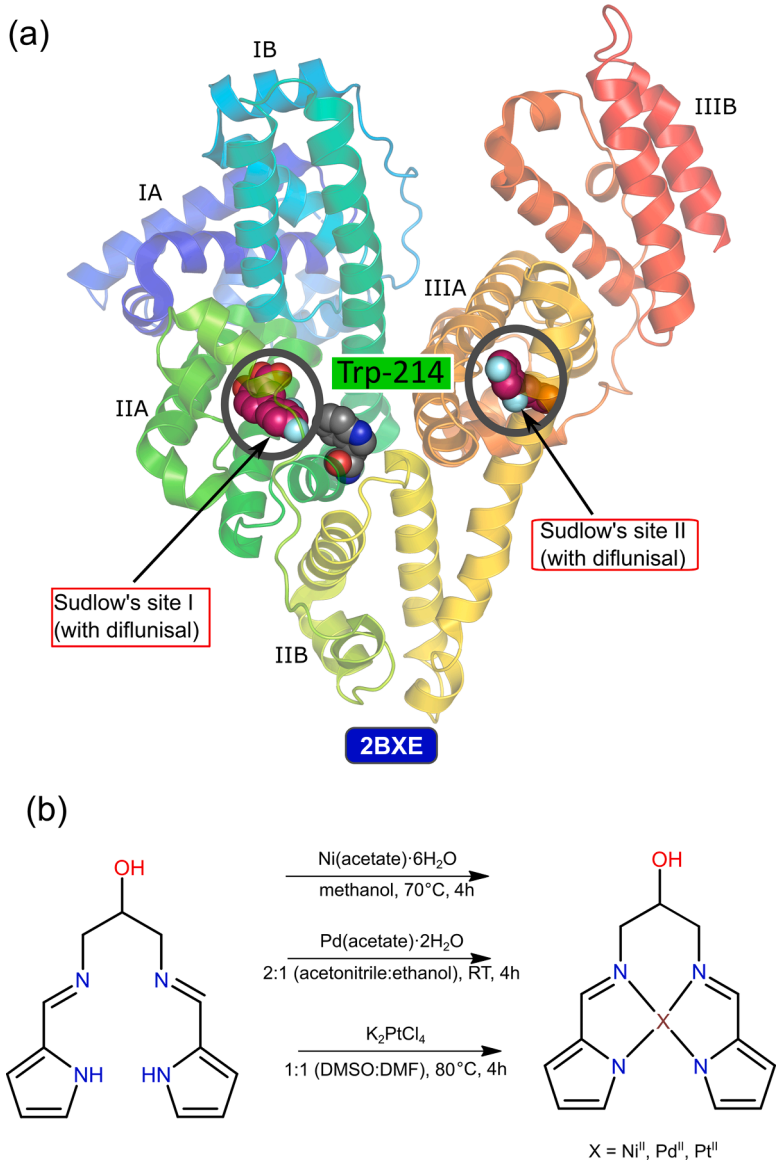

Scheme 1. (a) X-ray structure of HSA bound to diflunisal (redrawn from PDB code 2BXE [62]) illustrating the two main small molecule binding sites, Sudlow's site I and Sudlow's site II. The protein secondary structure elements are depicted schematically, coloured by domain, and labelled with Roman numerals and Arabic letters. H atoms (calculated positions) were added to both bound diflunisal molecules and Trp-214 to enhance their visualization. (b) Structures of the bis(pyrrole-imine) ligand H_2 L (1,3-bis(((E-1H-pyrrol-2-yl) methylene) amino) propan-2-ol) and a schematic synthesis procedure for the square planar d^8 metal ions relevant to this work; NiL, PdL, and PtL.

HSA's potential as a drug delivery system for anticancer agents, including paclitaxel [71], docetaxel and doxorubicin [72]. Elucidating the binding of metallodrugs to HSA is crucial for understanding their pharmacodynamic and pharmacokinetic profiles [59], and exploiting the enhanced permeability and retention effect of tumour tissue for targeted therapy.

As such, the versatility of d^8 Schiff base imine metal complexes offers fertile ground for designing next-generation cancer therapeutics with improved efficacy and reduced side effects. In this study, we synthesised 1,3-bis(((E-1H-pyrrol-2-yl) methylene) amino) propan-2-ol) and its corresponding isoelectronic (nd^8) square-planar chelates of Ni(II), Pd(II) and Pt(II) Scheme 1. Spectroscopic methods (fluorescence and UV-CD spectroscopy) were used to probe the binding of PdL by DNA and HSA under physiological conditions to gauge how the metal complex interacts with these macromolecules. Finally, *in silico* methods were used to corroborate the spectroscopic experimental data.

2. Results and discussion

2.1. Metal chelates synthesis and spectroscopic characterisation

The hydroxy pyrrole Schiff base ligand, H_2L, was synthesised straightforwardly by refluxing 1,3-diamino-2-propanol with pyrrole-2-carboxaldehyde (1:2) in ethanol [73]. Subsequent metalation of H_2L with hydrated nickel(II) and palladium(II) acetate salts in a 1:1 molar ratio, using methanol or ethanol as solvents, yielded isostructural Ni(II) and Pd(II) complexes (Scheme 1). The Pt(II) complex was synthesised using previously reported methods [73]. All metal complexes were purified via recrystallization and characterised by X-ray crystallography, revealing a novel crystal structure for PdL and a new structure for the previously reported NiL complex.

NMR spectroscopy. Recrystallized Schiff base complexes were used for spectroscopic characterization (Figs. S2–S11†). The ^{1}H NMR and electronic spectra for PdL are primarily presented and assigned in Fig. 1 to highlight the salient spectroscopic features of this class of compounds. The ^{1}H NMR spectrum of PdL (Fig. 1a) confirms coordination of the imine and pyrrole nitrogen's to the Pd^{II} ion by the tetradentate hydroxy

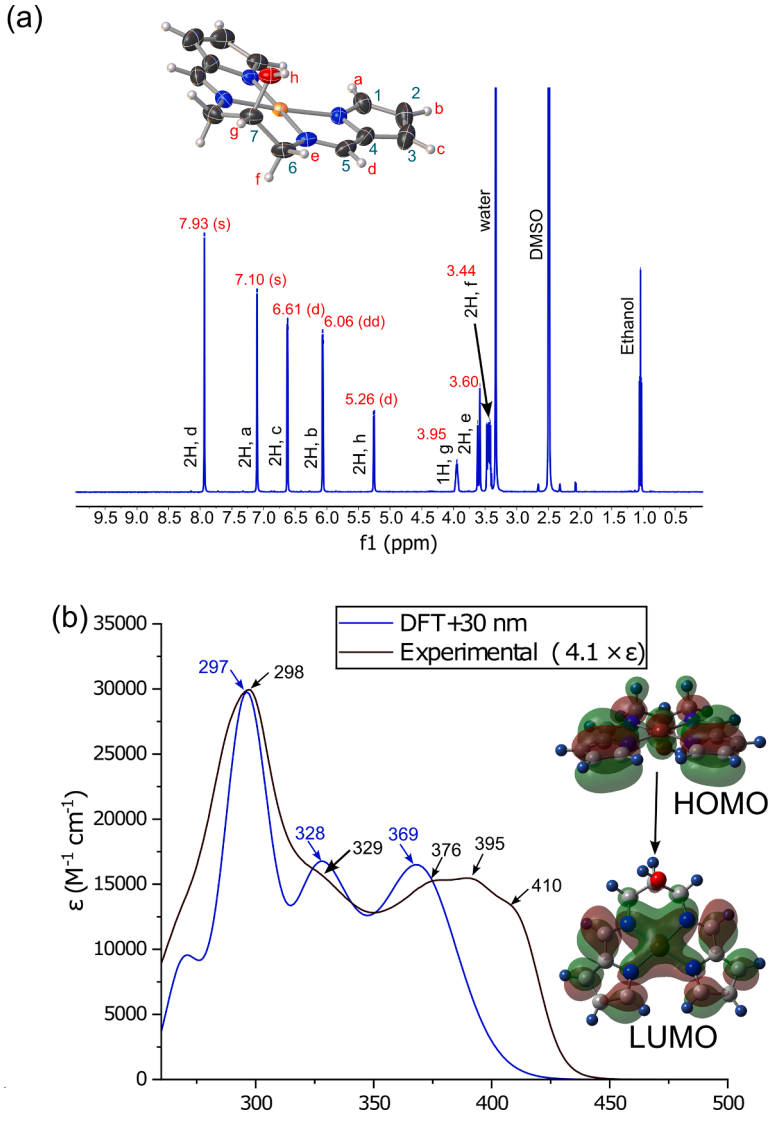

Fig. 1. Spectroscopic characterization and structural assignments for PdL. (a) Proton NMR spectrum (298 K, 400 MHz, DMSO-d_6). Labelled structure of PdL (top left) is a low temperature structure of the complex with the thermal ellipsoids rendered at 35 %, while the H atoms have an arbitrary radius. (b) Electronic spectrum of PdL recorded in acetonitrile. The TD-DFT calculated spectrum scaled (ε and λ) to best match the experimental spectrum is shown with selected transition assignments (band width = 2500 cm^{-1}, fwhm). The HOMO and LUMO frontier MOs are shown. A full list of transition assignments is given in Table S1.

bis(pyrrolide-imine) chelate. Characteristic features that highlight this are the disappearance of the pyrrole NH proton at 11.34 ppm and the imine proton (N=C–H) resonates at 7.93 (PdL) upfield from H_2 L (8.07 ppm). Notably, the imine proton (N=C–H) resonates as a singlet at 7.93 ppm in DMSO-d_6, exhibiting a downfield shift relative to NiL ($\delta_H = 7.60$ ppm) and an upfield shift compared to PtL ($\delta_H = 8.20$ ppm). A systematic trend emerges among the ^{1}H NMR chemical shifts of the imine proton across the d^8 metal ions, following the order: 3d (Ni) < 4d (Pd) < 5d (Pt). This trend suggests that the principal quantum number of the metal ion influences the shielding effect on the imine proton of the organic ligand framework, with increased electron density contributing to upfield shifts. Specifically, London dispersion forces (LDF) are implicated in the observed shifts, indicating a dependence on the metal ion centre's electronic properties [74,75].

The imine proton of NiL in Fig. S2 resonated at δ_H 7.60 ppm in DMSO-d_6, exhibiting an upfield shift of δ_H 0.31 ppm of the same complex in $CDCl_3$ (δ_H 7.29 ppm) [76]. This observation highlights the significant impact of solvent polarity on proton chemical shifts in this class of metal Schiff base chelates. Further insights into the solution-state structure of PdL were gained from its ^{1}H NMR spectrum. Two notable features were (i) a sharp doublet corresponding to the hydroxyl proton (h, Fig. 1a) (ii) distinct splitting patterns for the methylene protons in the ligand's alkyl bridge. The sharp hydroxyl proton signal indicates that intermolecular hydrogen bonding is reducing solvent-induced exchange broadening.

Electronic spectroscopy. The experimental UV–vis spectrum of PdL is presented in Fig. 1b and was assigned by analysis of the DFT-calculated spectrum of the Pd^{II} chelate. The DFT calculated electronic spectrum of PdL, which excludes vibronic transitions, is in fairly good agreement with the experimental UV–vis spectrum after application of a 30 nm red-shift correction to the band energies wavelength and a 4.1 factor scaling of the intensities of the experimental data (ε-values). The visible band at 395 nm is the first excited electronic state and is assigned to the HOMO → LUMO transition. The transitions are flanked by two shoulders at 376 and 410 nm, respectively, which are the corresponding transitions to the first excited vibrational level of the excited state. The energy of the DFT calculated first excited state at 369 nm 24 kJ mol^{-1} higher in energy. Analysis of the molecular orbitals (MOs) involved in the transitions of the first excited state indicated that it was composed of 80 % ^{1}[Pd($4d_{yz}$), π → Pd($4d_{xy}$), π* characteristic. The unoccupied MO are a mixture of metal-ligand wave function. The slightly more intense shoulder at a higher energy transition (329 nm) consisted of two major transitions H–3 → LUMO (38 %) and H–1 → L+1 (42 %). The far UV-region had the highest energy transition at 298 nm $\varepsilon = 1.58 \times 10^4$ M^{-1} cm^{-1} (experimental) corroborated with the 297 nm peak from the DFT calculated peak. The major MO transitions here were H–10 → L+2 and H–2 → L+7. These are low energy HOMO and high energy LUMO, furthermore the transitions are metal based and have mainly σ* character. Therefore, the 298 nm band is π → σ* character. Both transitions are significantly MLMLCT character (metal–ligand-to-metal–ligand charge transfer). The detailed electronic spectra for NiL and PtL have been previously reported [73,76].

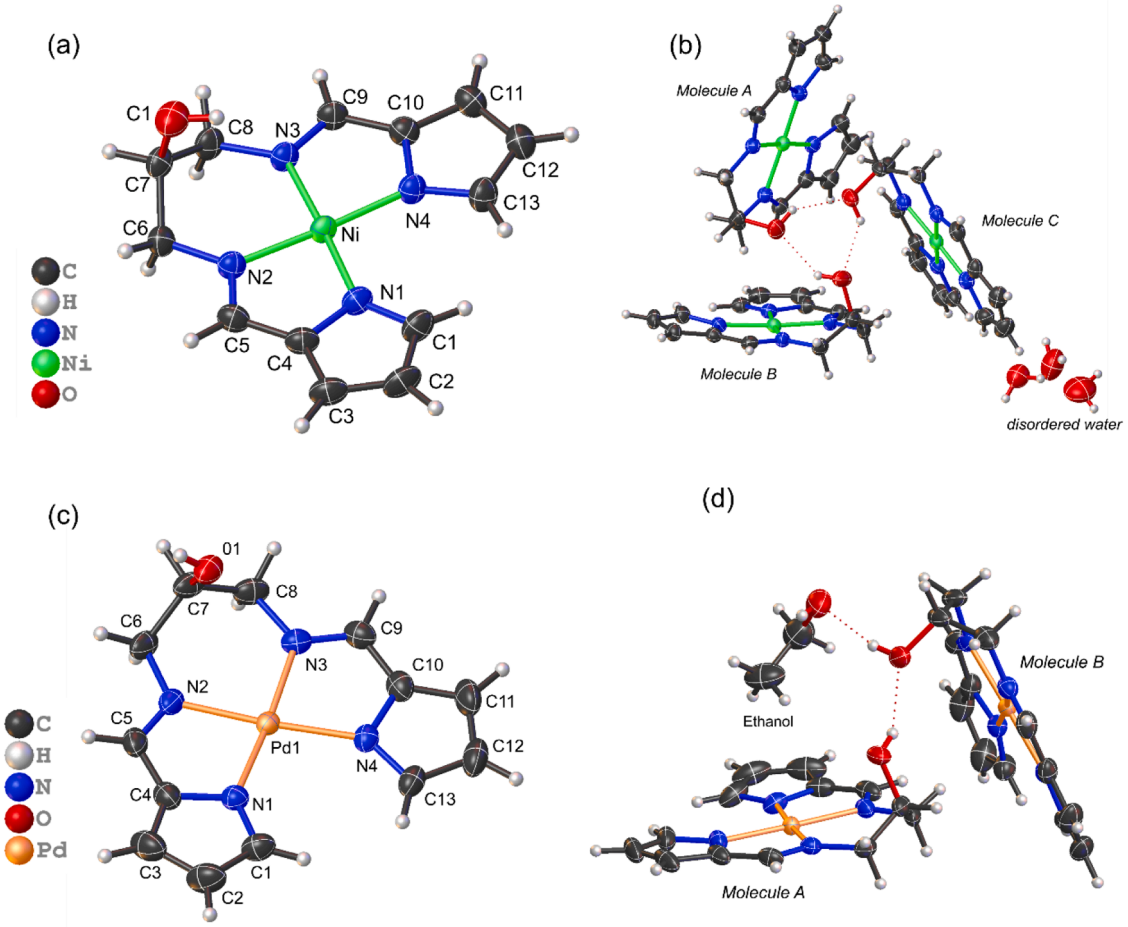

Fig. 2. (a) Labelled view of the low-temperature X-ray structure of NiL. One of the three independent molecules (molecule C) in the asymmetric unit is illustrated. (b) View of the asymmetric unit of the crystal structure of NiL with the three independent molecules forming an H-bonded trimer. (c) Labelled view of the low-temperature X-ray structure of PdL. One of two independent molecules in the asymmetric unit (molecule A) is illustrated. (d) View of the asymmetric unit of the crystal structure of PdL with the two independent molecules forming an H-bonded trimer with ethanol. Thermal ellipsoids are rendered at 35 % for all molecules and Hydrogen atoms are drawn as spheres with an arbitrary radius.

Single crystal X-ray diffraction (SC-XRD). The low temperature X-ray structures of NiL (crystallised with disordered water molecules) and novel PdL have been delineated and are presented in Fig. 2. Crystallographic data and refinement details are provided in Table S1 and Fig. S13. NiL crystallised in the triclinic space group P-1 (Table S2) and is structurally similar to the low temperature X-ray structure of the compound excluding ordered water molecules (Fig. S13) [76]. PdL also crystallised in the triclinic space group P-1. NiL contained three molecules and three ordered water molecules in the asymmetric unit (ASU), while PdL contained two molecules and an ethanol in the ASU, respectively. Both the Ni^{II} and Pd^{II} ions adopts the expected square planar geometry within the tetradentate chelate, as expected (Fig. 2a and c). However, the sum of the angles around the metal ion centres deviates slightly from the ideal value of 360°, with average values of 352.48 ±0.8° for Ni^{II} and 352.12 ±0.7° for Pd^{II}. This deviation is consistent with the constraints imposed by the chelate rings of the ligand. The slightly non-planar conformations of the metal complexes mainly indicate non-bonded crystal packing interactions and the formation of discrete, stacked dimers.

NiL and PdL exhibit Metal–Npyrrole distances of 1.898(19) and 2.011 (16) Å, respectively, while the Metal–Nimine distances were marginally longer (~0.1–0.4 %), measuring 1.907 (18) and 2.013 (16) Å for NiL and PdL, respectively. Longer Ni–Nimine bond lengths are typical for Ni(II) bis(pyrrolide-imine) chelates and has been previously reported for similar Ni(II) bis(pyrrolide-imine) Schiff base chelates [76, 77]. Interestingly, despite the presence of the ordered water molecules within the ASU data for the literature structure of NiL [76], which has mean Ni–Npyrrole and Ni–Nimine distances of 1.902(5) and 1.909(5) Å, respectively, the coordination group bonds are equivalent (within 1σ) to those determined at previously and is in agreement with the other NiII bis(pyrrolide-imine) chelates reported, [76,77] where the coordination group distances ranged from 1.877(4)–1.902(5). PdL was novel and could most suitably be compared to the low temperature structure of Pd (PrPyrr) [78]. Interestingly, the Pd–Nimine distances were longer than the Pd–Npyrrole distances for PdL while for Pd(PrPyrr) Pd–Npyrrole distances were longer than the Pd–Nimine distances. Selected bond lengths and bond angles are summarised in Table 1.

The ASU of NiL consists of three independent molecules that are linked to each other by hydrogen bonds (Fig. 2b), forming a trimeric supramolecular structure. The trimer was observed previously the reported structure of the ligand [76] and for the isoelectronic and isostructural Pt(II) derivative[73]. The non coordinated aliphatic hydroxy group facilitates as both a hydrogen bond acceptor and donor, which results in the formation of a six-membered H-bonded ring system (Fig. 2b). The trimeric supramolecular structure of NiL H-bonding lengths were 27 % shorter (2.021 ±0.07 Å) than the previously reported structure [76] (2.749 ±0.002 Å) and 8 % shorter than the Pt(II) analogue (2.18 ±0.01 Å) [73].

The ASU of PdL consisted of two mononuclear palladium complexes hydrogen bonded with an ethanol molecule. This resulted in an interesting supramolecular framework analysis account for an interesting role of ethanol through O···H interactions in assembling the complex units (Fig. 2d). The ethanolic-OH of the crystallised solvent and non-coordinated aliphatic-OH of the ligand backbone in PdL interacts very prominently through intermolecular O···H bonding 1.974 Å (ethanol···PdLwhile PdL O···H bonding distances were 2.014 Å leading to a dimeric framework (Fig. 2d).

Table 1
Selected mean crystallographic structural parameters for Ni[(OH)Pyrr] and Pd[(OH)Pyrr].

Bond distances (Å)	Ni[(OH)Pyrr]	Pd[(OH)Pyrr]
Metal–$N_{pyrrole}$	1.898(19)	2.0109(16)
Metal–N_{imine}	1.907(18)	2.013(16)
C=N	1.288(3)	1.295(3)
Bond angles (°)		
$N_{pyrrole}$Metal–$N_{pyrrole}$	105.4(2)	102.7(17)
N_{imine}–Metal–N_{imine}	93.15(8)	95.57(7)
cis–$N_{pyrrole}$–Metal–N_{imine}	84.21(8)	80.74(7)
trans–$N_{pyrrole}$–Metal–N_{imine}	175.78(8)	176.1(7)
C–$N_{pyrrole}$–C	113.5(2)	107.1(17)
C–N_{imine}–C	118.9(19)	121.7(16)

Parenthesis indicate standard deviation on the last significant figure.

2.2. Complex speciation

pH Speciation. The UV–Vis spectra of 50 μM solutions of PdL (pH 3.6–11.8) are presented in Fig. 3a. Across this pH range, a minimal decrease in absorbance was observed of 0.03, with the absence of isochoric points. These spectral changes were initially monitored at 369 nm and plotted as a function of pH (Fig. S18) and thought to be PdL ⇌ Pd[(H_2O)L at a pK_a value of 8.6 ±0.15. However, the TD-DFT calculated UV–vis spectra of Pd[(H_2O)L did not match that of PdL indicating that PdL did not undergo a speciation reaction as a function of pH and the only species present was PdL (at all measured pH's, and throughout this study). The drop in absorbance of 0.03 is attributed to the dilution of PdL in the constant ionic strength buffer with HCL.

The Pt^{II} ion was previously reported [73] to be complexed with H_2L, along with two other bis(pyrrolide-imine) ligands. All three Pt(II) complexes showed stability in an aqueous environment. This may be attributed to the fact that Pt(II) typically forms stronger metal-ligand bonds due to its higher effective nuclear charge compared to Pd(II), resulting in platinum complexes being more resistant to pH changes. In contrast, palladium complexes, due to their relatively weaker metal-ligand interactions, may be more susceptible to ligand hydrolysis (pyrrole, in this case) under similar conditions. Finally, NiL was not sufficiently stable and rapidly demetallated (Fig. S17).

Stability in serum. The stability of early-stage investigational drugs is important for a variety of reasons, such as if the drug will remain intact *in vivo* for a reasonable period to interact with the intended biomolecule target. Several metal drug candidates including cisplatin (Pt(II)), NAMI-A (Ru(II)), and Auranofin (Au(I)), has been reported undergo ligand exchange reactions, which causes the drug to interact with biomolecules as a simpler ionic metal species [79,80]. Both PdL (Fig. 3) and PtL [73] are stable over prolonged periods in an aqueous environment but have not been evaluated in serum. Therefore, the stability of PdL and PtL in human plasma was evaluated *in vitro* as a function of time by spectroscopy in the UV–visible region (Fig. 4). The absorbance maximum of each metal chelates had increased from 0 h to 3 h. This is likely due to the binding of the metal chelates to biomolecules within the human plasma,

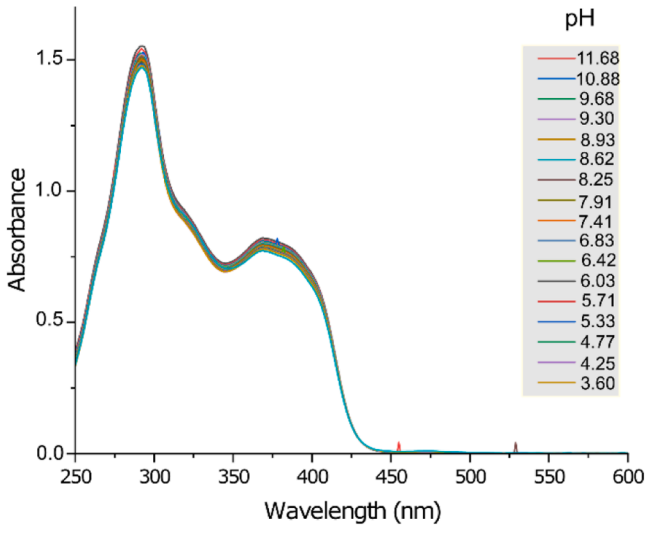

Fig. 3. (a) UV-visible spectra of PdL recorded as a function of pH at 37 °C.

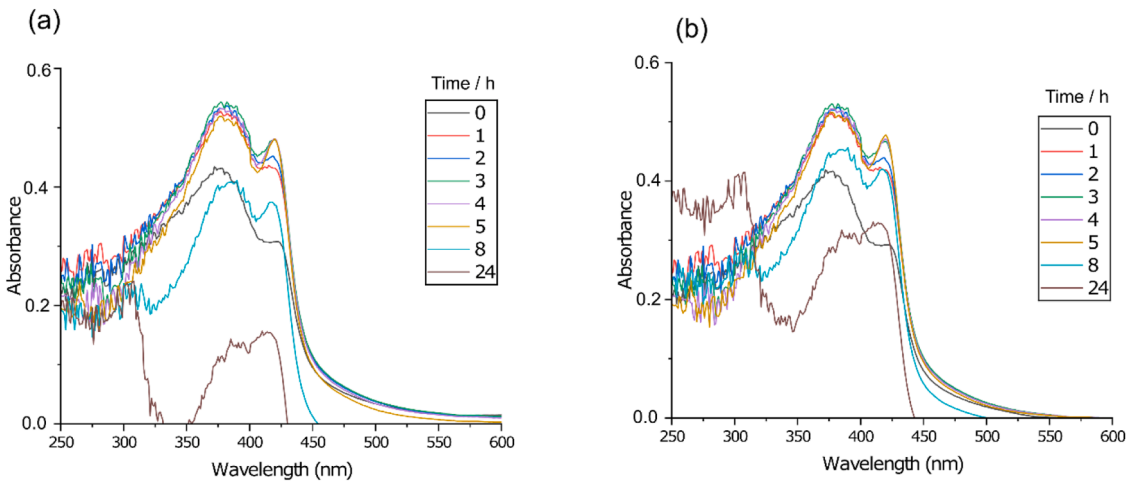

Fig. 4. Stability of (a) PdL and (b) PtL measured in human plasma. UV–visible spectral changes for both metal complexes (40 μM) recorded in a solution of human blood plasma diluted with phosphate buffer (50 mM KH2PO4, pH 7.50, 1:4 ratio) as a function of time.

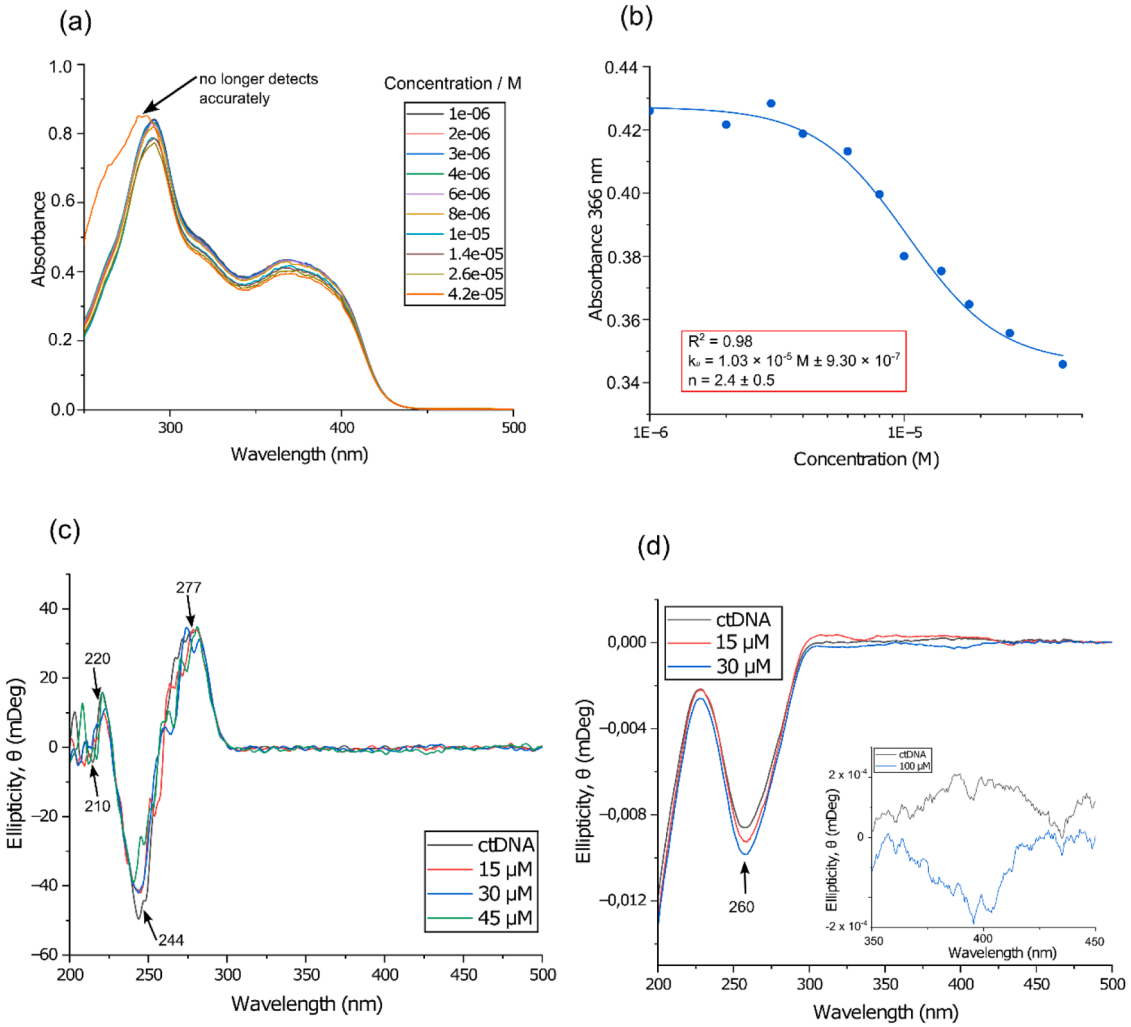

Fig. 5. (a) The UV–vis absorption spectra of PdL (50 μM) and (b) the change in the absorbance at 366 nm of PdL as a function of [ctDNA] fitted to the Hill model. The reaction was carried out in KH_2PO_4 (5 % (v/v) acetonitrile, 50 mM, pH 7.5) and after sequential additions of ctDNA (final [ctDNA] = 42 μM bp) the Hill fits were used to calculate the binding constants and stoichiometric ratios for the binding of PdL to ctDNA. Error bars indicate standard deviation of triplicate data. (c) The CD spectrum of 100 μM of ctDNA at increasing PdL concentrations in KH_2PO_4 (5 % (v/v) acetonitrile, 50 mM, pH 7.5) at 37 °C. The maxima and minima from 210 to 277 nm represent ctDNA and the 400 nm band represents an induced CD band due to the interaction of PdLwith ctDNA. (d) The LD spectrum of 100 μM ctDNA at increasing PdL concentrations in KH_2PO_4 (5 % (v/v) acetonitrile, 50 mM, pH 7.5) at 37 °C. The minimum at 260 nm represents ctDNA and the 350–450 nm broadened band represents an induced PdL LD spectrum.

such as DNA and human serum albumin [81]. Therefore, the metal chelates are now present in a more lipophilic environment and there are better band wavelength resolution (Fig. 4).

Both the Pd(II) and Pt(II) Schiff base chelates remained intact and unchanged for the first 5 h, there were no chemical changes such as bond dissociation or metal ion release were detected over the period. After which, there was a gradual decrease in band intensity throughout both the spectra. There were no isosbestic point formed or the formation of new bands. This indicates that demetallation did not occur but potentially the metal Schiff base chelates begun being hydrolysed (likely at the imine bond). Once the imine bond is hydrolysed, hydrolysis of the Schiff base chelate is enhanced, this is likely why hydrolysis occurred after 5 h [82,83]. The kinetics of the reaction could not be delineated from the current data set, as there was an increase in absorbance of the complex after 5 h, however, clearly from the UV–vis spectra we can deduce that $t_{1/2}$ will be greater than 12 h. This is comparable to drugs currently in circulation such as paclitaxel which has a reported plasma half-life of 6.54 ±1.43 h [84]. It should be highlighted at 24 h the band intensities do decrease to below 0 in some cases, this is attributed to precipitation of the complexes with the serum and potential increase in the turbidity of the serum solution.

3. DNA binding

The d^8 Schiff base imine metal complexes in this study were designed to target DNA as potential early-stage investigational compounds for cancer treatment. In this study, we did not have pharmacological data confirming that PdL can penetrate the cell membrane. However, low-resolution fluorescence microscopy images of a PdL analogue containing a Pt^{II} ion instead of Pd^{II} suggest that the chelate may enter the mitochondria [85]. Additionally, several other studies have reported metal Schiff base chelates that can permeate the cell membrane [86–88]. Based on previous literature ligand H_2 L chelating with Au^{III} was shown to target DNA as a therapeutic agent [89]. However, only PdL and PtL proved to be sufficiently soluble and stable for these actions. The H_2L ligand of the metal complexes has a planar structure and is anticipated that the compound will bind to and intercalate into the ctDNA. This was tested by measuring the binding affinity ($\boldsymbol{K_a}$), for PdL and PtL to calf thymus DNA (ctDNA) through UV-visible spectroscopic titrations. Fig. S14 indicated that PtL was not able to bind to the ctDNA. However, the MLCT absorption maximum band for PdL at 368 nm were monitored, and changes in the electronic spectrum at this wavelength indicated the interaction of PdL with ctDNA (Fig. 5). The highest obtained ratio of [ctDNA]:[PdL] before the end point was reached (i.e., precipitation of PdL), was 1:3.6.

The UV–vis spectrum in Fig. 5a indicates both hypochromism and hypsochromic (4 nm) as a function of PdL concentration. This is likely due to π–π* stacking interactions (vide infra) between the planar PdL and the base pairs of ctDNA. The blue shift suggests that PdL is positioned in a more apolar environment (i.e., indicating binding to DNA) and that there is a breakage of hydrogen bonds, that stabilise the secondary structure of ctDNA's double helix. The decrease in absorbance at 368 nm during the titration with ctDNA was fitted to the Hill model [90] yielding a R^2 value of 0.998 (Fig. 5b). This was used to delineate the affinity of PdL to ctDNA and was quantified by calculating the mean binding constant ($\boldsymbol{K_a}$) from three independent experiments: 0.114 (± 0.02) × 10^4 M^{-1}.

Typically, the binding affinity of intercalating compounds are lower than those of groove binders, and are below 10^5 M^{-1} [91,92]. The $\boldsymbol{K_a}$ for PdL (10^4 M) is lower than that of the ethidium bromide ($\boldsymbol{K_a}$ 1.5 ×10^6 M) the classical intercalating molecule. However, the is within the same camparable range as other reported square-planar palladium(II) intercalators [93–95]. The closest complex we can compare PdL to is with the Au^{III} analogue of the complex [89], which had a binding constant of 1.45 ×10^4 M^{-1}. This is 10 fold-higher than PdL and highlights the importance of the cationic metal ion centre.

The conformational changes of ctDNA in the presence of PdL was analysed using UV-CD spectroscopy (Fig. 5c). The native B-form DNA displays four principal transition bands at 210 nm, 220 nm, 244 nm, and 277 nm, respectively, which are indicative of its double-helical B-conformation [96,97]. The bands at 220 nm and 277 nm are associated with base stacking, while the bands at 210 nm and 244 nm are related to the helicity of DNA [96,98]. Upon the introduction of PdL to B-form DNA (ctDNA), the intensities of the 277 and 220 nm bands were minimally influenced by the ligand, while the 244 nm minima UV-CD, reduced as a function of PdL concentration. The result corroborates the hypochromic (4 nm) reported in Fig. 5a, indicating that PdL disrupted the hydrogen bonding network of ctDNA's secondary structure. Furthermore, the lack of peak changes indicate that ctDNA was not altered from B-form to A-form DNA as the characteristic 244 (B-form) maxima diminished in intensity and did not red-shift to A-forms DNA characteristic maxima at 263 nm [99].

The CD spectrum Fig. 5d indicates an interesting phenomenon between 400 and 450 nm, known as an induced circular dichroism (ICD) [100–103]. This occurs when an achiral molecule (PdL) binds to a macromolecular chiral host (ctDNA). This results in PdL perturbation, resulting in a net non-zero rotational strength, hence the emergence of a CD signal, referred to as ICD [102].

UV-LD was used to delineate the mode of binding of PdL to ctDNA [104]. The experiments were conducted in KH_2PO_4 buffer ((5 % (v/v) acetonitrile, 50 mM, pH 7.5), with 100 μM ctDNA and varying concentrations of PdL (0–300 μM). The LD spectrum of ctDNA exhibited a strong negative signal at 260 nm, attributed to the nucleotides (purine and pyrimidine base pairs) [104] of ctDNA. Upon the addition of PdL, there was a concentration-dependent increase in the amplitude of the 260 nm minima (Fig. 5d), suggesting enhanced DNA rigidity (i.e., DNA stiffening) and implying either an elongation and/or increased rigidity of the double-helical DNA. This result indicates that the DNA is intercalated and subsequently unwound (Fig. 5d) [105–107].

Additionally, an induced dichroic signal was detected between 350 and 450 nm (Fig. 5d inset). At this wavelength range, there is no contribution from DNA base pairs; only the chromophore PdL absorbs in this region. Since PdL is isotropic and cannot be oriented in the flow field, the presence of the ICD signal corroborates the ICD signal in Fig. 5c (UV-CD) and indicates that PdL forms a molecular complex with ctDNA, becomes oriented, and intercalates into DNA. The ICD signal, being below the plane of native ctDNA, further confirms that PdL and was replicated with ethidium bromide (Fig. S15).

3.1. Molecular docking and molecular dynamic simulations

Theoretical ligand docking studies were employed using Glide XP to determine the binding mode of PdL to DNA. Two DNA X-ray structures were used; PDB: 425D (2.80 Å) [108] and PDB: 4E1 U (0.92 Å) [109], for flexible ligand docking. It should be noted that ligand docking provides only an approximation as to how a ligand may bind to and interact with DNA. The major parameter elucidated from ligand docking are the docking scores, which typically do not correlate quantitatively with experimental binding or thermodynamic data ($\boldsymbol{K_a}$ or ΔG values) [110,111]. This is because ligand docking does not try to emulate a physical reaction between the incoming ligand and macromolecule. Hence, only qualitative comparisons can be made from docking scores. In our case we aim to determine if Glide XP docking scores corroborates our experimental data and shows PdL intercalating with DNA

The key results are that two PdL bind to the oligonucleotide, this is expected since DNA has repeating AT and GC regions, therefore multiple potential binding sites may host the incoming ligand with similar affinity. It should be highlighted that since the PDB structures of DNA are rigid and have been crystallised in the presence of either a groove binder (PDB: 425D) or an intercalator (PDB: 4E1 U), the binding scores for complex PdL were solely used as a theoretical approach to support experimental data.

Glide XP docking of PdL to the oligonucleotide revealed that the complex has a preference for PDB 4E1 U (intercalating oligonucleotide) (Table 2) as it exhibits a more favourable ΔG_{bind} score as compared to PDB 425D The lowest best docked ΔG_{bind} score was in fact higher than the highest best docked score ΔG_{bind} score from PDB: 4E1U. The result corroborates the experimental data (vide supra), which indicates that PdL is an intercalator of DNA. Furthermore, the Glide XP docking data suggests that PdL may bind and intercalate at the central 5′-AT-3′ step of the oligonucleotide (Fig. S16), though with a relatively low Glide docking score (ΔG_{bind} = –5.30 kcal/mol). As expected the AT cluster sites are the preferred binding locations, because they have been shown to exhibit the lowest binding energy [112].

Following ligand docking of the PdL complex to the DNA oligonucleotide (PDB: 4E1 U), a 100 ns molecular dynamics (MD) simulation (Fig. 6) was conducted to assess the stability of the best Glide XP docking pose (Fig. S16). MD simulations provide valuable insights into the interactions between macromolecules and ligands over time, capturing the system's dynamic behaviour and offering a more accurate reflection of physiological conditions. As shown in Fig. 6, the root-mean-square deviation (RMSD) of PdL remains relatively stable throughout the simulation trajectory (deviating between 0.25–0.75 Å). However, the significance of the slight deviations in the ligand's RMSD are highlighted in Fig. 6. At the start of the 100 ns simulation, two PdL molecules are bound to the oligonucleotide. PdL (1; black) is bound to DG(8) and DT (3), while the second metal complex (blue) is bound to DA(5), DC(10), and DG(3). GC pockets are higher in energy and often less favourable sites for molecules to bind and intercalate. Consequently, throughout the trajectory, both Pd^{II} chelates exhibit changes in their binding positions (this can be visualised using MD, as MD forcefields allow for more dynamic interactions.

At 84 ns a minimum is reached between both Pd^{II} chelates and the DNA oligonucleotide and it is observed that both molecules are hydrogen bonded to the DT nucleic acids and no longer within a pocket, that was observed at 24 ns. Between 24 ns and 84 ns the minimal deviations in the RMSD are attributed to the Pd^{II} chelates re-orientating into the DNA strand that has now being unwound due to intercalation from the PdL molecules. This insertion of both PdL residues into the oligonucleotide strands base pairs results in the displacement of the stacked base pairs and initiates DNA uncoiling [113]. At the end of the 100 ns simulation, the DNA structure undergoes significant unwinding, disrupting the electrostatic interaction between PdL and the nucleic acids (Fig. 6). These MD simulation results are consistent with the experimental UV-LD data in Fig. 5d, where the increase in the 260 nm minimum amplitude indicates ctDNA unwinding in response to increasing PdL concentration. It should be noted that due to the limitations of the Maestro Suite (2022–4), DNA-specific RMSD and root-mean-square fluctuation (RMSF) values could not be calculated, requiring reliance on the trajectory output to infer ligand binding.

In our investigation, the correlation of data from spectroscopic binding experiments, UV-LD, UV-CD experiments, and computational studies on the interaction between PdL and DNA all corroborated that the primary mechanism of interaction is intercalation. MD simulations (Fig. 6) indicate that the OH moiety of PdL binds to pyrimidine base pairs via hydrogen bonding, while the pyrrole nitrogen interacts through electrostatic interactions. Finally, the purine base pairs form π–π bonds with PdL's pyrrole rings. Therefore, we propose that the first binding state involves π–π bonding between PdL's pyrrole rings and the purine base pairs, followed by hydrogen bonding and electrostatic interactions, ultimately leading to the intercalation of ctDNA. This intercaltions results in the unwinding of ctDNA. Similar binding mechanisms have been previously reported for other Schiff base Pd^{II} complexes [114,115].

Table 2
Summary of GLIDE XP docking scores and selected interaction energy parameters for DNA targets prepared from ligand-free structures derived from PDB codes 425D (biased towards groove binding), 4E1 U (biased towards intercalating). The docking runs were truncated to report only the top-scoring ligand pose for each ligand. All energies are in units of kcal mol^{-1}.

PDB	Binding site residues	XP Gscore	Glide Energy
PDB:425D	AT	–4.21	–26.23
PDB: 4E1U	AT	–5.30	–34.53

3.2. Fluorescence quenching measurements

The interaction of potential pharmaceutical compounds (PdL in this study) with plasma proteins is a key factor in determining their bioavailability [116]. Assessing plasma protein binding is essential when evaluating potential therapeutic agents. In particular, the interaction of these compounds with human serum albumin (HSA), a vital transport protein in the circulatory system, is of significant importance. HSA can bind to a wide range of both endogenous metabolic compounds and externally administered drugs. This binding interaction plays a crucial role in regulating the concentration of free drug, thereby influencing its availability and activity within the body [117]. The intrinsic fluorescence for a protein can be quenched by different mechanisms, namely static, dynamic, or a combination of both. The protein in this study HSA, has a single Trp residue (Trp-214, λ^{ex} = 295 ***nm***) located in Sudlow's site I that is responsible for most of the protein's intrinsic fluorescence emission [118]. The quenching of the intrinsic emission spectrum of HSA (310–450 nm) was investigated by the titration of varying concentrations of PdL into the protein and the emission maximum was observed at ~342 nm. The fluorescence intensity of HSA decreased monotonically as a function of PdL concentration (Fig. 7a). The fluorescence spectroscopic data indicates that PdL binds in close proximity to Trp-214 and alters the microenvironment around the fluorophore and inducing a marked dose-dependent quenching of the intrinsic fluorescence of HSA [119,120].

PdL induced a blue shifts relative to the native protein of 5 ±0.2 nm, which reflects the development of a significantly less polar environment around Trp-214 after the Pd^{II} complex uptake [78]. The blue-shift observed here is in agreement with the similarly reported Pd(PrPyrr) molecule that induced a blue shift of 5.4 ±0.4 nm, when bound to HSA [78] and differs from the Pt(II) class of molecules with the same ligand which all induced red shifts relative to native HSA [73]. This highlights that for HSA, the wavelength of the fluorescence λ^{em}_{max} is dependent on the identity of the metal ion.

The observed blue shift in the fluorescence of the Trp fluorophore can be attributed to two main factors: (i) the orientational polarization caused by ordered water molecules located within 15–25 Å of the residue and (ii) the electronic polarization of the Trp indole ring itself. In the context of HSA•{complex}, the electronic polarization of Trp-214, influenced by the bound ligand, alongside the disruption of the ordered water structure surrounding the chromophore, likely contributes to these shifts. This is especially relevant when considering the electronic properties of PdL bound close to the lone Trp-214 residue in the protein. The direction of the shift whether blue or red will depend on the orientation and the distance between the ligand's dipole moment and the transition dipole moment associated with the lowest energy $^1A_1$ to ^1La transition of Trp's indole ring [119]. This transition is characterised by transient charge migration from the pyrrole to the benzene ring of the chromophore. Ultimately, the specific binding configuration of the ligand within subdomain IIA of HSA will determine both the sign and magnitude of λ^{em}_{max}.

3.3. Fluorescence quenching mechanism

Stern-Volmer model. Fluorescence quenching is normally described by the Stern-Volmer (SV) equation (Eq. (1)) [121].

$$\boldsymbol{I}_0/\boldsymbol{I} = 1 + \boldsymbol{K_{SV}}[\boldsymbol{Q}] = 1 + \boldsymbol{k_q}\boldsymbol{\tau}_0[\boldsymbol{Q}] \quad (1)$$

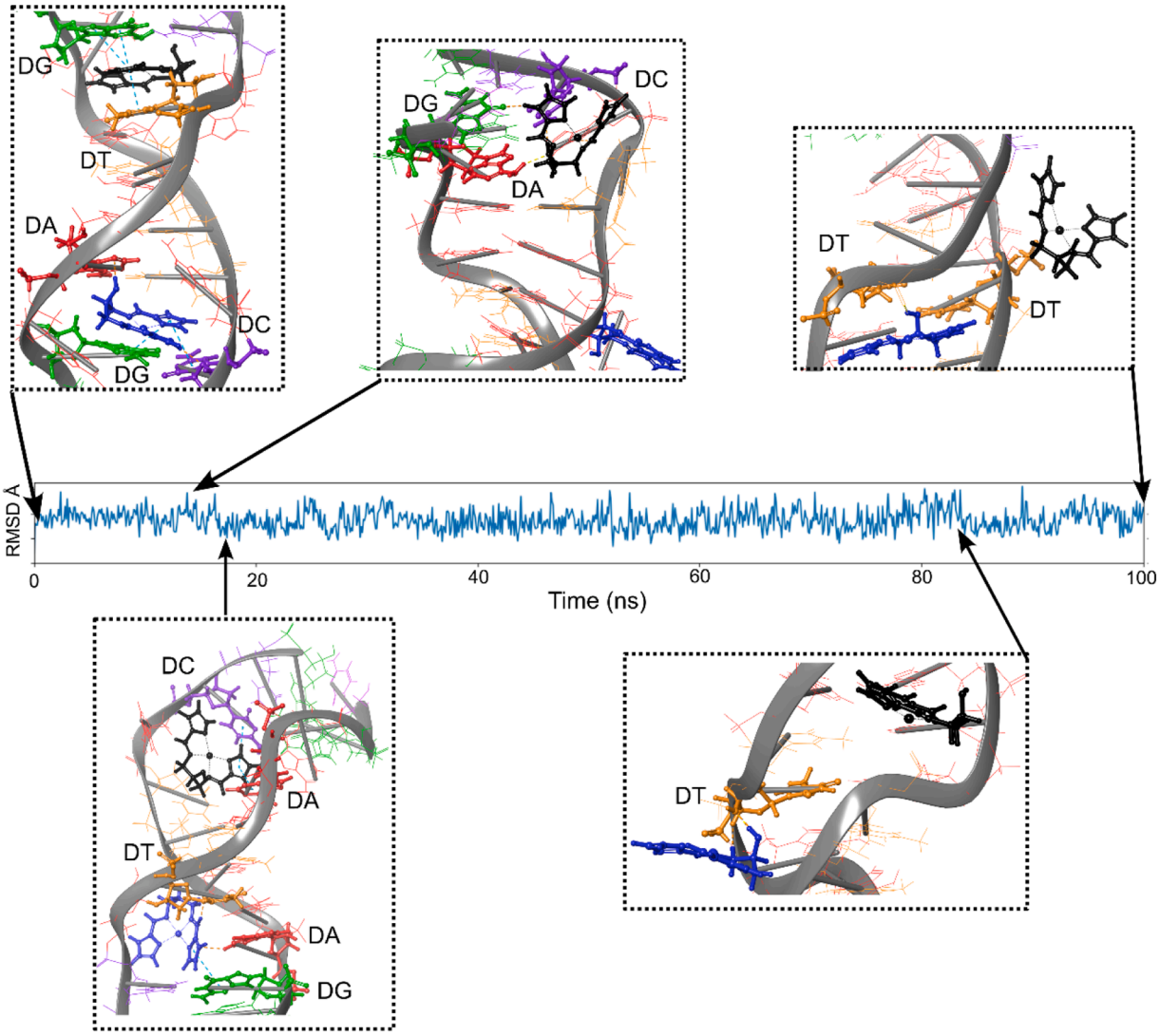

Fig. 6. Molecular dynamic simulation (MD) over 100 ns of the best docked GLIDE XP structure of complex PdL binding to an oligonucleotide of DNA (PDB 4E1 U; 5′-D(CGGAAATTACCG)−3′ bound with a cationic ruthenium complex $[Ru(bpy)_2(dppz)]^{2+}$) [109]. A large target grid was generated for ligand docking at the $[Ru(bpy)_2(dppz)]^{2+}$) site close to the centre of the DNA(with $[Ru(bpy)_2(dppz)]^{2+}$) removed), spanning 40×40×40 $Å^3$, thereby facilitating a search of alternative binding packets radiating throughout the oligonucleotide. (a) The RMSD indicates that there is minimal fluctuation of complex PdL throughout the MD run, however, image docked poses of the fluctuation of PdL is presented bound within the best XP docked sites. Nucleic acid base pairs are colour coded Adenosine (red), Thymine (orange), Cytosine (purple) and Guanosine (green). RMSF and RMSD data of triplicate results is presented in Figs. S21 and S22.

where $\boldsymbol{I}_0$ is the fluorescence intensity of ligand free HSA (PdL in this work) and $\boldsymbol{I}$ is the fluorescence intensity of HSA in the presence of PdL. $\boldsymbol{K_{SV}}$ is the Stern-Volmer constant (M^{-1}), $[\boldsymbol{Q}]$ is the molar concentration of the quencher, $\boldsymbol{k_q}$ is the bimolecular quenching rate constant (M^{-1} s^{-1}), and $\boldsymbol{\tau_0}$ is the average lifetime of HSA fluorescence in the absence of any quencher (5.28 ±0.03 ns [122], 5.60 ±0.10 ns [123], 6.72 ±0.07 ns [124]; mean = 5.87 ±0.76 ns). SV plots recorded as a function of temperature and [PdL] are presented in Fig. 7b. The plot indicates the average of triplicate results of the mean fluorescence ratio recorded at each dose of PdL complex. Typically, Eq. (1) is linear for a single dominant quenching mechanism, either dynamic or static, the SV plot for PdL is observed to follow a single dominant quenching mechanism. Notably, the $\boldsymbol{K_{SV}}$ values of PdL decreased with increasing temperature, consistent with a static quenching mechanism.

From least-squares fits of Eq. (1) to the dose-dependence of $\boldsymbol{I}_0$ /$\boldsymbol{I}$, the bimolecular fluorescence quenching rate constant for the HSA•{PdL} complex can be straightforwardly deduced from Eq. (2), with the reported $\boldsymbol{\tau_0}$ value (vide supra).

$$\boldsymbol{k_q} = \boldsymbol{K_{SV}}/\boldsymbol{\tau_0} \quad (2)$$

The values of $\boldsymbol{K_{SV}}$ and $\boldsymbol{k_q}$ determined here for the interaction of native HSA with PdL ~2 to ~10 times larger than, for instance, those reported for HSA interacting with berberine [125], epinastine hydrochloride [126], primethamine and trimethoprim [127],. However, is similar to the isostructural PtL ($\boldsymbol{K_{SV}}$ = 1.16 ×10^{-5} ±0.1 M^{-1}; $\boldsymbol{k_q}$ = 2.27 ×10^{-13} M^{-1} s^{-1} at 310 K) [101], and M(PrPyrr) (M = Ni^{II}, Pd^{II} or Pt^{II}), where $\boldsymbol{K_{SV}}$ ranged from 1.34 to 2.52 ×10^{-5} M^{-1} and ranged $\boldsymbol{k_q}$ = 2.28–4.30 ×10^{-13} M^{-1} s^{-1} at 310 K [78]. A comparison of the isostructural complexes showed that the $\boldsymbol{K_{SV}}$ for PdL > PtL. This is because PdL low-lying excited states overlapping the emission from Trp-214 are $^1(\pi–\pi^*)$ excited states and two metal chelate species simultaneously bind to the protein, which statistically increases the quenching. PtL is phosphorescent, and has a singlet excited state $^1(\pi–\pi^*)$ that relax by internal conversion and intersystem crossing to the lowest-energy emissive triplet excited state, $^3(\pi–\pi^*)$ [27,128].

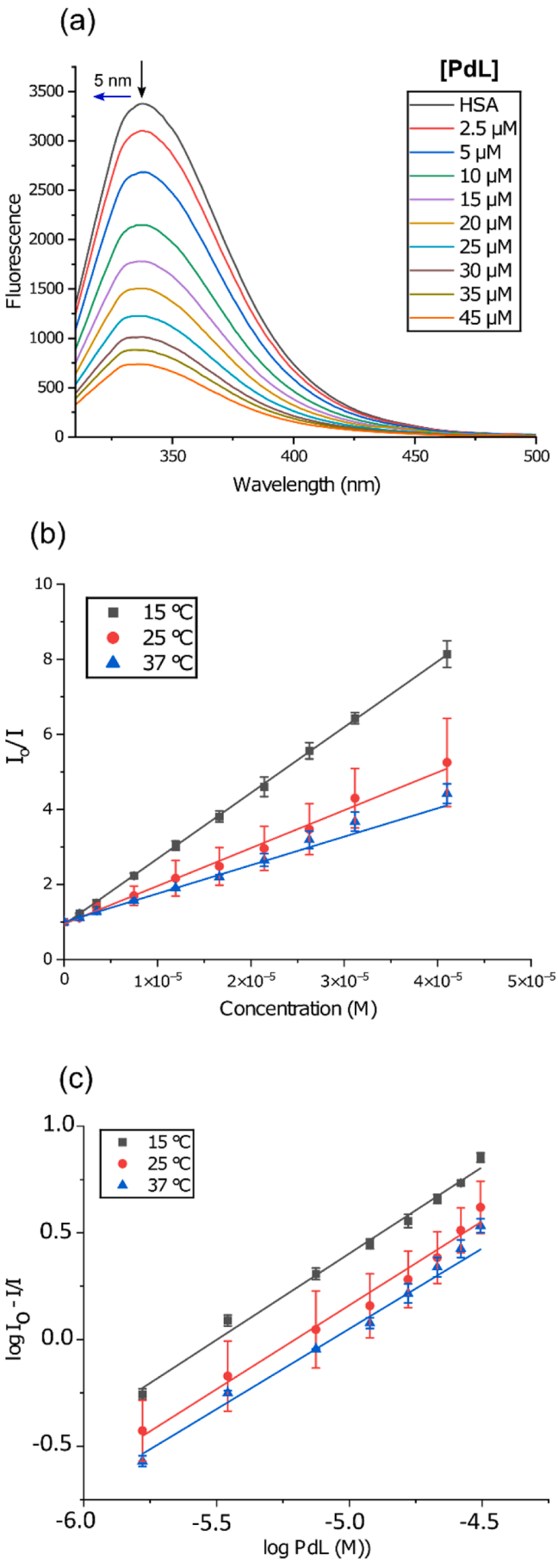

(caption on next page)

Fig. 7. (a) Emission spectra of HSA (4.0 μM) recorded as a function of the concentration of PdL at 298 K in KH_2PO_4 (50 mM, pH 7.50). (b) Stern-Volmer (SV) fluorescence intensity ratio plots for HSA (4.0 μM) recorded as a function of the concentration of PdL and temperature (50 mM KH_2PO_4, pH 7.50). Error bars are ESD's based on the average of three independent determinations. (c) Double logarithm plot of the fractional change in fluorescence intensity for HSA (4.0 μM) recorded as a function of the concentration of PdL and temperature (50 mM KH_2PO_4, pH 7.50). Error bars are ESD's based on the average of three independent determinations. The data are described by Eq. (3), which affords the affinity constant and stoichiometric coefficient for the reaction (Table 3).

Table 3
Stern–Volmer quenching constants (K_{SV}), bimolecular quenching rate constants (K_q), and affinity constants (log K_a) for the interaction of PdL with HSA at different temperatures in 50 mM KH_2PO_4 buffer at pH 7.50.

Compoud	T (K)	**Ksv** (x105)	**Kq** (x10 − 13)	**logKa**	n
	288	1.62 (0.0085)	2.76	4.45 (0.14)	1.21 (0.01)
PdOH	298	0.94 (0.17)	1.60	4.10 (0.22)	1.18 (0.04)
	310	0.773 (0.05)	1.32	3.82 (0.25)	1.10 (0.05)

[a] K_{SV} values were determined by fitting the data to nonlinear Eq. (2) to the data. [b] A mean excited state lifetime, τ_o, of 5.87(76) ns for HSA was used to calculate the bimolecular quenching rate constant, K_q. [c] The estimated standard deviations of the least significant digits are given in parentheses.

3.4. Ligand binding equilibrium constants

Changes in HSA fluorescence intensity as a function of [PdL] was used to calculate thermodynamic data for the binding equilibrium between the Pd^{II} complex and HSA. The biophysical parameters that describe the ligand's affinity for the protein (K_a) and the stoichiometry of the reaction (n) are delineated from a log plot of the emission data as a function of increasing PdL concentration (Eq. (3)) [129].

$$log\left(\frac{I_0 - I}{I}\right) = logK_a + nlog[Q] \quad (3)$$

where the intercept and slope of the curve give the affinity constant and stoichiometry, respectively. The data is summarised in Table 3. The results show that the affinity constant decreases with increasing temperature, consistent with a static quenching mechanism [130,131].

The value of $logK_a$ for the PdL chelate ranges from 4.45 to 3.82 (288–310 K) and is akin to the product equilibrium constant β_2, where $log\beta_2 = logK_1 + logK_2$. It is noteworthy that K_1 and K_2 for the reaction of HSA with PdL are *unresolvable* (distinct binding steps are not observed in the titration data, Fig. 7d). Furthermore, the binding of PdL is distinct and specific to PdL alone. The closest Pd^{II} complex to which we can compare its affinity is Pd(PrPyrr), with $logK_a = 5.52$[78]. However, Pd(PrPyrr) was prone to hydrolysis at all pH levels, resulting in the removal of the pyrrole group from the Pd^{II} ion centre. The binding of Pd(PrPyrr) was therefore a result of the interaction between Pd(PrPyrr) and Pd(OH_2Pyrr). Thus, PdL is unique in that it does not undergo hydrolysis and is more stable than other imine Pd^{II} Schiff base chelates.

3.5. Thermodynamics of ligand binding

PdL had a linear van't Hoff relationship, and the plot for triplicate measurements are given in Fig. 8a. Under non-standard conditions, the enthalpy change (ΔH), entropy change (ΔS), and Gibbs free energy change (ΔG), may be deduced from the temperature dependence of the affinity constants (K_a) using Eqs. (4) and (5):

$$lnK_a = -\frac{\Delta H}{RT} + \frac{\Delta S}{R} \quad (4)$$

$$\Delta G = \Delta H - T\Delta S \quad (5)$$

Table 4 summarises the thermodynamic data for reaction of the

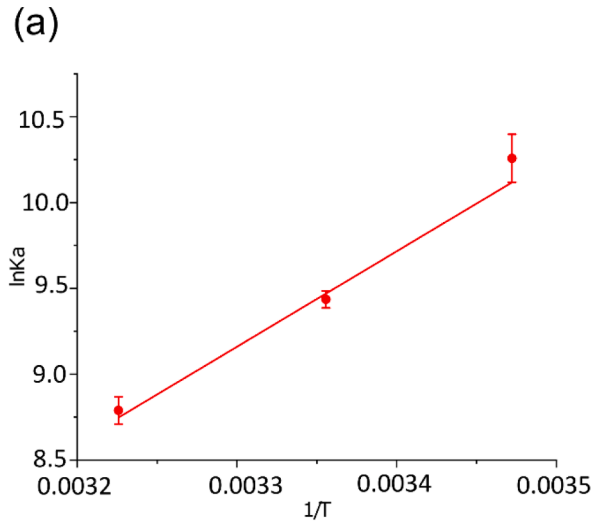

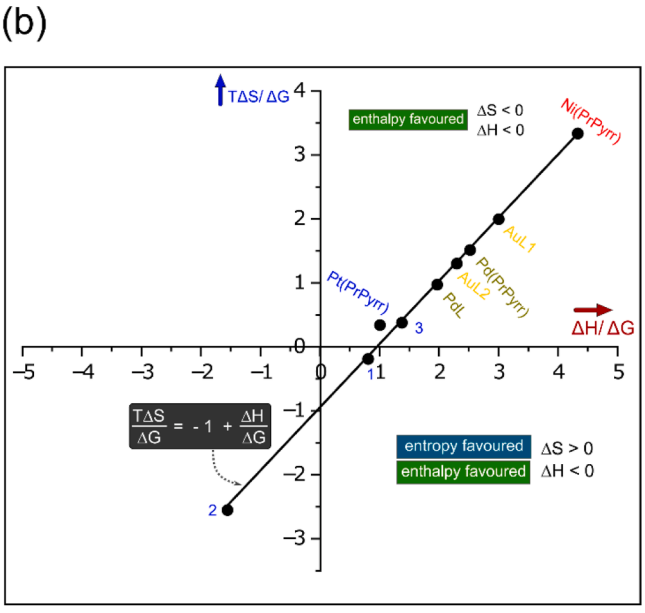

Fig. 8. (a) Linear van't Hoff plots for the reactions of PdL with HSA in 50 mM KH_2PO_4 buffer at pH 7.50. (b) Plot of the Gibbs-Helmholtz relationship (Eq. (9)) for the reaction of Pd[(OH)Pyrr] and different metal imine Schiff base chelates [73,78,132] binding to HSA at 298 K for comparison in 50 mM KH_2PO_4 buffer at pH 7.50. The straight line fit of the data gives $R^2 = 0.997$ with a slope and intercept of –1. For all reactions, $\Delta G < 0$. Error bars indicate the standard deviation of three independent results.

Table 4
Thermodynamic parameters for the binding of PdL, by HSA in 50 mM KH_2PO_4 buffer at pH 7.50.

Compound	T (K)	ΔG kJ mol^{-1},[a]	ΔH kJ mol^{-1},[a]	ΔS j K mol^{-1},[a]
PdL	288	24.2 (2)	–46.3 (6)	–76 (2)
	298	23.4 (2)		
	310	22.5 (3)		

[a] The estimated standard deviation are given in parentheses.

compounds of interest with HSA in KH_2PO_4 buffer. The reaction is exergonic [129], with ΔG ranging from −24.2–22.5 kJ mol^{-1} from 288 to 310 K. The much ΔG is in a similar range to that reported for the Pt(II) cogner [73].

The enthalpy (ΔH) value for the reaction is –46.3 (6) kJ mol^{-1}, indicating it is exothermic; however, it is almost twice that of PtL –26.2 (2.7) [73]. Since the main drug binding sites known are Sudlow's sites I and II (subdomains IIA and IIIA) in the protein are mostly hydrophobic [133], the favourable heats of reaction suggest that there is minimal disruption of the protein's ordered water or backbone structure and that LDF of attraction are mainly responsible for binding of the present ligands in these sites. This notion is indeed confirmed by our molecular docking simulations (vide infra).

By using the Gibbs-Helmholtz relationship (Eq. (5)) with the experimental data (Table 4), the thermodynamics governing PdL uptake by HSA was delineated (Fig. 8b). Specifically, when $T\Delta S/\Delta G$ is plotted against $\Delta H/\Delta G$, a linear data fit is observed in the top right quadrant of the graph where $\Delta H < 0$, consistent with enthalpic control of the reaction. Here, spontaneity is assured as changes in ΔH /ΔG are compensated for by commensurate changes in $T\Delta S/\Delta G$. In Fig. 8b we compared the Gibbs-Helmholtz relationship of PdL with our previously reported Schiff base chelates [73,78,132]. Strikingly, all nine metal chelates followed a linear trend $R^2 = 0.997$, however, only the group 10 neutral metal complexes $T\Delta S/\Delta G$ and $\Delta H/\Delta G$ increased together in the order: Ni(PrPyrr) < Pd^{II}(X) < Pt^{II}(X), which follows the increase in the principal quantum number for the metal ion (3d < 4d < 5d).

The trend suggests that the thermodynamics of metal chelate binding to HSA are influenced by the increasing electron density in the complexes, which naturally occurs as the size and polarizability (i.e., softness) of the metal ion increase [134,135]. LDF of attraction in biomolecules significantly control the tertiary structure of the macromolecule [136], and will increase in the order 3d < 4d < 5d [135] for this class of Schiff base pyrrolide-imine metal chelates, Fig. 8b demonstrates that LDF attraction governs the interaction of the current metal chelates with HSA largely by modulation of the ΔH term. The square planar Au^{III} chelates were the exception to the trend of the group 10 neutral metal complexes. Even though they fitted the Gibbs-Helmholtz fit, it is likely that the overall negative charge on the complexes influenced their binding to HSA.

The ΔS of PdL binding to HSA was –76.4 JK^{-1} mol^{-1}, significantly higher than that of PtL binding to HSA (18.5 jK^{-1} mol^{-1}). This is likely influenced by two PdL molecules being present, which ultimately

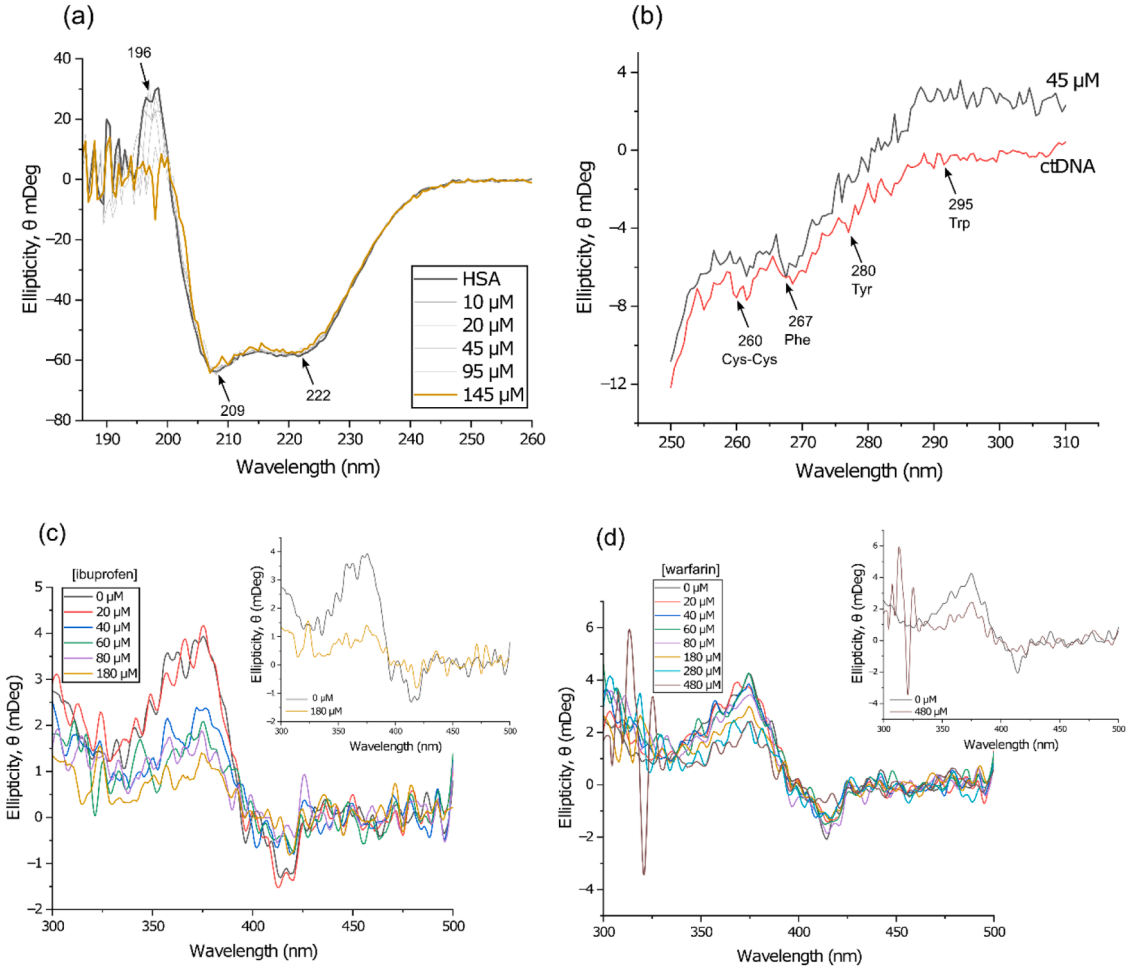

Fig. 9. (a) Plot of the far-UV CD spectra of native HSA and the protein incubated with saturating doses of PdL recorded at 310 K in 50 mM KH_2PO_4 buffer at pH 7.50. The plot is unsmoothed spectra at PdL doses ranging from 0 to 145 μM. Grey spectra indicate concentrations of 10, 20, 45 and 95 μM of PdL. Band minima are indicated. (b) Plots of the UV-visible CD spectra of native HSA (15 μM) and the protein incubated with a saturating dose (145 μM) of PdL were recorded at 310 K in 50 mM KH_2PO_4 buffer at pH 7.50. Perturbations in the protein structure around Phe (250–270 nm), Tyr (~280 nm), and Trp (285–300 nm) residues may also be resolved in some difference spectra. Selected wavelengths in the UV CD spectrum are marked. Induced CD site displacement assay carried out by measuring the UV–vis CD spectrum of HSA (15 μM in 50 mM KH_2PO_4 buffer, pH 7.5) bound to PdL (15 μM). The site-specific markers warfarin (Sudlow's site I) and ibuprofen (Sudlow's site II) were titrated into the solution of HSA•2{PdL} in Parts (c) and (d), respectively, at concentrations of 0–180 μM or 0–450 μM. The assay identifies which probe drug or marker can displace the Pd(II) chelate from its target binding site and thus delineates the exact binding site of the metal chelate within the protein. The spectra were smoothed using a Lowess function (0.10 span) for clarity.

displaces more ordered water molecules and results in a higher ΔS. Overall PdL binding thermodynamics here are similar data reported from microcalorimetry studies on drugs that target Sudlow's site II, the binding of drugs such as benzodiazepines [137], ibuprofen [138], and phenothiazines by HSA [139], that had moderately negative ΔH (−50 to −75 kJ mol^{-1}) and ΔS values as well as sizeable K_{a1} values ~10^5 M^{-1} [140]. Warfarin, which binds in Sudlows's site [141] has broadly comparable thermodynamics [140] ($logK_{a1}$ = 5.15, ΔH = −49 kJ mol^{-1}, ΔS = −12 J K^{-1} mol^{-1}) to ibuprofen (Sudlow's site II, $logK_{a1}$ = 5.04, ΔH = −67 kJ mol^{-1}, ΔS = −34 J K^{-1} mol^{-1}) indicating that assigning the specific binding site of PdL requires additional structural or spectroscopic data.

Investigational equilibrium studies on HSA and PdL have been conducted and are reported in the ESI (Fig. S23) according to methods previously reported [142]. From the ICD competition assay and in silico methods (vide infra), we know that HSA binds to PdL in a 1:2 ratio. However, due to the poor solubility of PdL at concentrations above 10-fold the concentration of HSA, we were unable to clearly elucidate the second binding constant or reach complete saturation of HSA (Fig. S23). Therefore, for the equilibrium HSA + PdL ⇌ HSA{PdL}, we calculated aK_a of 0.40×10^4 M^{-1} and a K_d of 2.53×10^{-4} M at 310 K. The binding equilibrium allows us to calculate the dependence of HSA on PdL concentration. These calculations enabled us to determine the average number of PdL molecules bound to HSA, yielding a value of 1.2 ±0.05, which indicates that more than one PdL molecule binds to HSA and corroborates the UV–ICD studies.

3.6. UV-CD spectroscopy

Far-UV circular dichroism (CD) spectroscopy is a method typically employed to analyse changes in a protein's secondary structure (i.e., α-helices, β-sheets, and random coils) upon small molecule binding [143,144]. The impact of PdL on HSA's secondary structure was measured over the 186–260 nm range (Fig. 9a). The CD spectrum of HSA in the absence of Pd(II) complex displayed two minima at 209 (±1 nm) and 222 nm (±1 nm), which is characteristic of an α-helical rich protein (Fig. 9a). The electronic transitions for both minima are attributed to π–π* (209 nm) and n–π* (222 nm) excitations, respectively and the 196 nm π–π* maxima [143]. All three transitions originate from the amide bonds of the peptide backbone [143,144].

The far-UV CD spectrum of HSA in the presence of PdL was similar to that of complex-free HSA, with only a minimal decrease in ellipticity (Fig. 9a) between 200 and 260 nm. However, the 196 nm maxima ellipticity had completely diminished. PdL exhibited moderately high binding affinities for HSA (Table 3), affecting CD intensity changes only around 196 nm. Overall, PdL minimally affected the overall secondary structure of HSA, even at concentrations as high as 145 μM.

The far-UV CD data were further analysed using JASCO Spectra Manager™ to calculate the percentage composition of the secondary structure elements present for the HSA• PdL adduct. The dominant secondary structure domains are α-helices (~56 %), turns (~11 %), and unordered coils (~32 %). It has been previously reported that the secondary structure composition of HSA differs from that of native HSA in

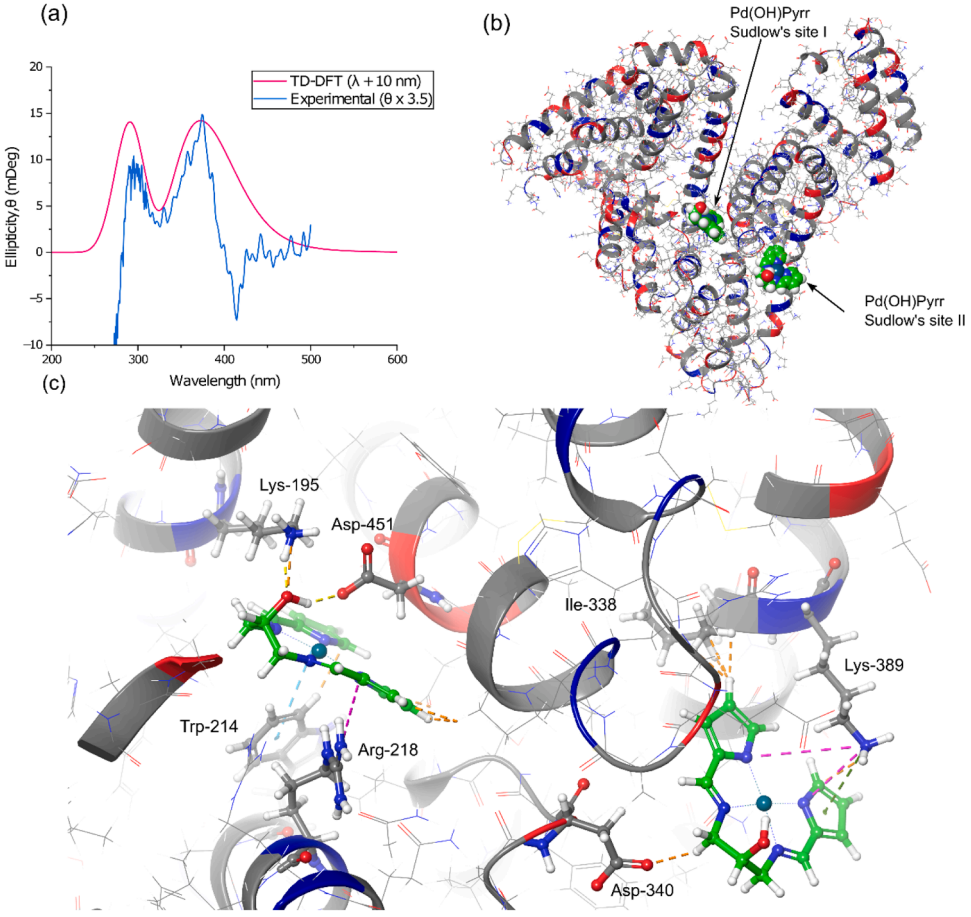

Fig. 10. (a) Comparison of the experimental ICD spectrum (Δθ) recorded for HSA•{Pd(OH)Pyrr} at pH 7.5 in 50 mM (KH_2PO_4) and the CD spectrum calculated using hybrid QM:MM TD-DFT simulations (CAM-B3LYP/SDD/GD3BJ:UFF) for the top-scoring docked pose of Pd(OH)Pyrr bound to both Sudlow's site I and Sudlow's site II (PDB code: 1HA2). The DFT-calculated spectrum of the best pose matches the experimental spectrum with great accuracy. (b) Structural model used for the TD-DFT simulations showing the location of both Pd(OH)Pyrr molecules bound within Sudlow's sites I and II. (c) View of the metal chelate binding site containing the best pose of both Pd(OH)Pyrr and the closest amino acid residues interacting with the Pd^{II} chelates.

the solid state [133] (68.5 % α-helix, 0 % β-sheet, 9.6 % turns, and 21.9 % unordered coils; PDB code 1BM0 analysed with BeStSel [145]). However, the CD data present here is consistent with solution-state spectral decompositions previously reported [146–148]. It is widely accepted that increased subdomain mobility and overall thermal motion or disorder contribute to the reduction in α helicity [144,149].

The influence of PdL on the tertiary structure of HSA was investigated through near-UV CD spectroscopy (Fig. 9b). This probes the electronic structure of Trp (285–300 nm), Tyr (275–285 nm), and Phe (250–270 nm), and allows for the examination of conformational changes in the protein's tertiary structure. The near-UV CD spectrum of HSA in the absence of any ligands typically shows two minima at 260 and 280 nm and a maximum at 290 nm due to disulphide bonds and aromatic amino acids [150]. Perturbations between 250 and 310 nm provide insights into the conformational changes occurring in HSA. Trp residues have a higher quantum yield and lower symmetry compared to Phe and Tyr, therefore it is most sensitive to changes within the immediate microenvironment [151]. The three aromatic amino acid residues have $\pi \rightarrow \pi^*$ transitions (^1L_a and ^1L_b) and may be involved in π bonding. Furthermore, the $\pi \rightarrow \pi^*$ transitions exhibit charge transfer characteristics, making them sensitive to dielectric changes in the chromophore microenvironment; consequently, variations in the solvent can influence these transitions [152]. Therefore, alterations in the near-UV CD spectrum can be correlated with tertiary structure changes for HSA in the presence of ligand binding or as a result of solvent exposure perturbing the aromatic residue's microenvironment [153].

Near-UV CD spectra were recorded from 250 to 310 nm for HSA• PdL (Fig. 9b). The perturbation at 295-nm is attributed to the Trp ^1L_b (0,0) band, while the overlapping Tyr and Trp bands are observed at 260–280 nm (^1L_a; solvated Trp) [154,155],. When PdL is bound to HSA, these marker perturbations exhibit a significant positive change in ellipticity with wavelength shifts of ± 2 nm. The perturbation alterations suggests that both Tyr and Trp are more solvent exposed and may be influenced by the electrostatic field of the Pd(II) complex. This accounts for the minor alterations in the secondary structure of HSA (Fig. 9a), i.e., the decrease in α-helicity around 196 nm.

To investigate the site-specific binding of PdL to HSA, an induced circular dichroism (ICD) site displacement assay was conducted. PdL was incubated with HSA in a KH_2PO_4 buffer (50 mM, pH 7.5), followed by titration with either warfarin (a Sudlow's site I probe) or ibuprofen (a Sudlow's site II probe). Since PdL is achiral, it does not produce a CD signal unless bound to a chiral macromolecular host, such as HSA. If warfarin or ibuprofen displaces PdL from its binding site, the ICD signal of PdL diminishes, indicating the metal chelate has returned to its achiral, unbound state in solution.

As shown in Fig. 9c, the ICD spectrum of the HSA•PdL complex was not completely diminished by the addition of warfarin, even at excessive amounts of warfarin (as high as 480 μM). Approximately 38 % of PdL was displaced from HSA's Sudlow's site I. Notably, the logK_a value of PdLfor HSA is 5.43 at 310 K, which is comparable to that of warfarin for the protein (5.5). This indicates that Sudlow's site I was one of the primary binding sites for the Pd(II) complex, but not the only one. At the highest warfarin concentration (480 μM), the appearance of the warfarin- induced CD peak at 306 nm was observed, signifying a HSA•warfarin adduct forming. In Fig. 9d, when ibuprofen was titrated into HSA• PdL there was a monotonic decrease in the ICD signal from PdL within HSA, which indicates the displacement of PdL by ibuprofen into the aqueous buffer and thus confirming that PdL bound in either one or both ibuprofen binding sites (subunits IIIA or between IIA and IIIA) [27].

The evidence collectively demonstrates that PdL and PtL, previously reported [73] prefer binding in Sudlow's site II (subdomain IIIA). The data suggests that PdL preferentially binds to Sudlow's site II, and once the site is saturated, excess ligand binds to Sudlow's site I, since more Pd (II) chelates was displaced from Sudlow's site II. Theoretical *in silico* data (ONIOM, TD-DFT simulations) provided corroborative information for the preferential binding of PdL within Sudlow's site II of HSA by matching the key features of the experimental CD spectrum (Fig. 9). Despite compelling spectroscopic evidence, however, only X-ray or cryo-electron microscopy data can delineate the precise binding site(s) of PdL with absolute certainty.

Insights from DFT simulations. Based on our *in silico* docking data obtained, we used hybrid QM:MM TD-DFT simulations (ONIOM method [156]) to calculate the ICD electronic structures of HSA•2{PdL} with the Pd(II) chelates (Fig. 10) occupying both Sudlow's sites I and II. The best two poses indicated that PdL binds to Sudlow's site II and then Sudlow's site I and was taken directly from the optimised Glide XP structure (Fig. 10) was assigned to the quantum mechanics (QM) layer. Amino acid residues from Sudlow's site II were Ile-338, Lys-389 and Asp-340, while the amino acid residues from Sudlow's site I were Lys-195, Trp-214, Arg-218 and Asp-451, all were added to the QM layer for the most accurate ICD spectrum calculation (Fig. 10a). HSA's amino acid residues were simulated using MM (UFF [157]). The TD-DFT calculated ICD spectrum of HSA•2{PdL} strikingly resembled the key spectral features of the experimental ICD spectrum with only a 10 nm spectral wavelength correction. The simulations strongly indicate that PdL occupies both Sudlow's sites. Furthermore, the docking Fig. 10b and c highlight that PdL bound to Sudlow's site I is in direct contact with Trp-214 and that can account for (i) FRET-based quenching of this amino acid and (ii) location of the ligand within 5.9–12 Å of at least one Tyr residue. This also supports the sphere of action model (vide supra).

4. Conclusions

PdL was found to be stable under physiological pH's and had only undergone pyrrole dissociation above pH 8.6. Unlike its Ni(II) and Pt(II) congers PdL, was able to bind to DNA through intercalation as MOA. This was confirmed by spectroscopic methods (UV-LD-spectroscopy) and corroborated by theoretical MD simulations. Interestingly, this suggest that PdL has the potential to be an early-stage investigational therapeutic agent. Finally, PdL binding to HSA was investigated by complementary spectroscopic techniques to understand how the complex binds to the protein. It was found to quench HSA's intrinsic Trp-214 fluorescence of HSA via a static quenching mechanism. Furthermore, we report that two intact PdL complexes bind to HSA in Sudlow's sites I and II. *In silico* data supported the notion (gleaned from spectroscopy) that two PdL molecules bound to HSA minimally perturbs the protein's secondary structure. Finally, the induced CD spectra recorded for the metal chelates bound to HSA strikingly confirm uptake of the intact complexes.

Approval of the submitted version of the manuscript

Please check this box to confirm that all co-authors have read and approved the version of the manuscript that is submitted. Signatures are not required.

CRediT authorship contribution statement

Sheldon Sookai: Writing – review & editing, Writing – original draft, Visualization, Project administration, Methodology, Investigation, Funding acquisition, Formal analysis, Data curation, Conceptualization. **Ayanda Majoka:** Methodology, Formal analysis, Data curation. **Manuel A. Fernandes:** Formal analysis, Data curation. **Monika Nowakowska:** Supervision, Conceptualization.

Declaration of competing interest

The authors declare that they have no known competing financial interests or personal relationships that could have appeared to influence the work reported in this paper.

Acknowledgements

The authors thank WITS University and the NRF for funding to purchase a JASCO J-1500 MCD spectrometer (Grant No 116177, OQM) and a Dual-Wavelength Bruker D8 Venture X-Ray Diffractometer (Grant No 129920, OQM). We also thank the Centre for High Performance Computing (Project CHEM1633, CHPC, Cape Town) for both the CPU time and resources needed for the DFT simulations.

Supplementary materials

Supplementary material associated with this article can be found, in the online version, at doi:10.1016/j.molstruc.2025.141880.

Data availability

Data will be made available on request.

References

[1] C.E. Hewton, M.C. Kimber, D.K. Taylor, A One-Pot Synthesis of Thiophene and Pyrrole Derivatives from Readily Accessible 3,5-Dihydro-1,2-Dioxines, Tetrahedron Lett. 43 (2002) 3199–3201, https://doi.org/10.1016/S0040-4039(02)00503-8.

[2] R.U. Braun, K. Zeitler, T.J.J. Müller, A Novel One-Pot Pyrrole Synthesis via a Coupling−Isomerization−Stetter−Paal−Knorr Sequence, Org. Lett. 3 (2001) 3297–3300, https://doi.org/10.1021/ol0165185.

[3] B. Sahu, R. Sahu, B. Gidwani, A. Mishra, Pyrrole: An Essential Framework in the Development of Therapeutic Agents and Insightful Analysis of Structure-Active Relationships, ChemistrySelect 9 (2024) e202401604, https://doi.org/10.1002/slct.202401604.

[4] N. Jeelan Basha, S.M. Basavarajaiah, K. Shyamsunder, Therapeutic Potential of Pyrrole and Pyrrolidine Analogs: An Update, Mol. Divers. 26 (2022) 2915–2937, https://doi.org/10.1007/s11030-022-10387-8.

[5] A.M. Abu-Dief, N.M. El-Metwaly, S.O. Alzahrani, A.M. Bawazeer, S. Shaaban, M. S.S. Adam, Targeting ctDNA Binding and Elaborated In-Vitro Assessments Concerning Novel Schiff Base Complexes: Synthesis, Characterization, DFT and Detailed in-Silico Confirmation, J. Mol. Liq. 322 (2021) 114977.

[6] L.H. Abdel-Rahman, M.S. Adam, A.M. Abu-Dief, H.E.-S. Ahmed, A. Nafady, Non-Linear Optical Property and Biological Assays of Therapeutic Potentials under in Vitro Conditions of Pd (II), Ag[(I) and Cu (II) Complexes of 5-Diethyl Amino-2-({2-[(2-Hydroxy-Benzylidene)-Amino]-Phenylimino}-Methyl)-Phenol, Molecules 25 (2020) 5089.

[7] K. Al-Ghamdi, M.M.A. Alharas, S.A. Abdel-Latif, D. Alhashmialameer, E.S. Al-Farraj, M.A. Almalki, R.M. El-Khatib, A.M. Abu-Dief, Selective Novel Metal-Coordinated Biomedical Agents Encompassing Tetradentate Salen Ligand: Structural Elucidation, DFT Calculation, Cytotoxic, and Antioxidant Activities Supported by Molecular Docking Approach, Appl. Organomet. Chem. 39 (2025) e7991, https://doi.org/10.1002/aoc.7991.

[8] A.M. Abu-Dief, Y. Al-hawamy, A. Abdou, A.H. Alsehli, B.M. Altayeb, A. Alqurashi, G.G. Mohamed, Design, Synthesis, Structural Inspection, and DFT Calculation of Some Novel Imine Ciprofloxacin Metal Chelates: A Novel Approach for Pharmaceutical Applications and DNA Interaction, Appl. Organomet. Chem. 38 (2024) e7637, https://doi.org/10.1002/aoc.7637.

[9] K. Hüttinger, C. Förster, T. Bund, D. Hinderberger, K. Heinze, Stereochemical Consequences of Oxygen Atom Transfer and Electron Transfer in Imido/Oxido Molybdenum(IV, V, VI) Complexes with Two Unsymmetric Bidentate Ligands, Inorg. Chem. 51 (2012) 4180–4192, https://doi.org/10.1021/ic202588u.

[10] A.M. Kadhum, S.H. Mallah, A.S. Waheeb, A.W. Salman, A. Zafar, N.S. Ahmad, S. Siraj, M.A. Iqbal, Advancement in Schiff Base Complexes for Treatment of Colon Cancer, Rev. Inorg. Chem. (2024), https://doi.org/10.1515/revic-2024-0068.

[11] K.R.N. Bhowmik, Biomedical Applications of Some Schiff Bases and Their Transition Metal Complexes: A Review, Asian J. Chem. 36 (2024) 2485–2500, https://doi.org/10.14233/ajchem.2024.32594.

[12] M.A. Rhine, A.V. Rodrigues, R.J.B. Urbauer, J.L. Urbauer, T.L. Stemmler, T. C. Harrop, Proton-Induced Reactivity of NO^- from a $\{CoNO\}^8$ Complex, J. Am. Chem. Soc. 136 (2014) 12560–12563, https://doi.org/10.1021/ja5064444.

[13] S.A. Carabineiro, L.C. Silva, P.T. Gomes, L.C.J. Pereira, L.F. Veiros, S.I. Pascu, M. T. Duarte, S. Namorado, R.T. Henriques, Synthesis and Characterization of Tetrahedral and Square Planar Bis(Iminopyrrolyl) Complexes of Cobalt(II), Inorg. Chem. 46 (2007) 6880–6890, https://doi.org/10.1021/ic062125w.

[14] D. Bandyopadhyay, M. Layek, M. Fleck, R. Saha, C. Rizzoli, Synthesis, Crystal Structure and Antibacterial Activity of Azido Complexes of Cobalt(III) Containing Heteroaromatic Schiff Bases, Inorg. Chim. Acta 461 (2017) 174–182, https://doi.org/10.1016/j.ica.2017.02.018.

[15] M.R. Walter, S.P. Dzul, A.V. Rodrigues, T.L. Stemmler, J. Telser, J. Conradie, A. Ghosh, T.C. Harrop, Synthesis of Co^{II} –NO^- Complexes and Their Reactivity as a Source of Nitroxyl, J. Am. Chem. Soc. 138 (2016) 12459–12471, https://doi.org/10.1021/jacs.6b05896.

[16] H. Brunner, B. Nuber, T. Tracht, Optically Active Transition Metal Complexes. Part 119:New Rhodium(I) Complexes Containing Two Different Types of Optically Active Ligands, Tetrahedron: Asymmetry 9 (1998) 3763–3771, https://doi.org/10.1016/S0957-4166(98)00389-9.

[17] H. Brunner, A. Köllnberger, M. Zabel, Optically Active Transition Metal Complexes. Part 133. Preparation, Epimerization and Crystallization of Chiral-at-Metal Rhodium(III) Half-Sandwich Complexes, Polyhedron 22 (2003) 2639–2646, https://doi.org/10.1016/S0277-5387(03)00346-2.

[18] S. Basu, I. Pal, R.J. Butcher, G. Rosair, S. Bhattacharya, Rhodium and Iridium Complexes of N-(2′-Hydroxyphenyl)Pyrrole-2-Aldimine: Synthesis, Structure, and Spectral and Electrochemical Properties, J. Chem. Sci. 117 (2005) 167–173, https://doi.org/10.1007/BF03356112.

[19] Y. Haketa, M. Miyasue, Y. Kobayashi, R. Sato, Y. Shigeta, N. Yasuda, N. Tamai, H. Maeda, Self-Associating Curved π-Electronic Systems with Electron-Donating and Hydrogen-Bonding Properties, J. Am. Chem. Soc. 142 (2020) 16420–16428, https://doi.org/10.1021/jacs.0c07751.

[20] P. Paul, M.G. Richmond, S. Bhattacharya, Iridium-Mediated N–H and Methyl C–H Bond Activations in N-(2′,6′-Dimethylphenyl)Pyrrole-2-Aldimine. Synthesis, Characterization and Catalytic Applications, J. Organomet. Chem. 751 (2014) 760–768, https://doi.org/10.1016/j.jorganchem.2013.07.066.

[21] C.H. Wei, J.R. Einstein, Structure of a Bis-Bidentate Metal Complex, Bis-(*N* - *t* -Butylpyrrole-2-Carbaldimino)Nickel(II). Analysis of Its Configurational Disorder in the Crystalline State, Acta Crystallogr. B Struct. Sci. 28 (1972) 2591–2598, https://doi.org/10.1107/S056774087200651X.

[22] Y. Wang, H. Fu, F. Shen, X. Sheng, A. Peng, Z. Gu, H. Ma, J.S. Ma, J. Yao, Distinct M and P Helical Complexes of H_2 O and Metal Ions Ni^{II}, Cu^{II}, and Zn^{II} with Enantiomerically Pure Chiral Bis(Pyrrol-2-Ylmethyleneamine)Cyclohexane Ligands: Crystal Structures and Circular Dichroism Properties, Inorg. Chem. 46 (2007) 3548–3556, https://doi.org/10.1021/ic062316z.

[23] S. Bhikraj, O.Q. Munro, M.P. Akerman, An Unusual Asymmetric Pseudomacrocyclic Free Base Ligand and Nickel(II) Chelate: X-Ray Crystallographic and DFT Studies, Polyhedron 124 (2017) 22–29, https://doi.org/10.1016/j.poly.2016.12.026.

[24] J.S. Hart, G.S. Nichol, J.B. Love, Directed Secondary Interactions in Transition Metal Complexes of Tripodal Pyrrole Imine and Amide Ligands, Dalton Trans. 41 (2012) 5785, https://doi.org/10.1039/c2dt30539a.

[25] H. Liang, J. Liu, X. Li, Y. Li, Synthesis, Structure and Norbornene Polymerization Behavior of Neutral Palladium Complexes, Polyhedron 23 (2004) 1619–1627, https://doi.org/10.1016/j.poly.2004.03.017.

[26] C.N. Iverson, C.A.G. Carter, R.T. Baker, J.D. Scollard, J.A. Labinger, J.E. Bercaw, C−H Bond Activation by Unsymmetrical 2-(*N* -Arylimino)Pyrrolide Pt Complexes: Geometric Effects on Reactivity, J. Am. Chem. Soc. 125 (2003) 12674–12675, https://doi.org/10.1021/ja036511d.

[27] X.-F. Shan, D.-H. Wang, C.-H. Tung, L.-Z. Wu, C–H···Pt(II) Interaction-Controlled Self-Assembly and Photophysics of Chiral Bis(Pyrrol-2-Ylmethyleneamino) Cyclohexane Platinum(II) Complexes, Tetrahedron 64 (2008) 5577–5582, https://doi.org/10.1016/j.tet.2008.03.077.

[28] Y. Kim, J. Lee, Y.-H. Son, S.-U. Choi, M. Alam, S. Park, Novel Nickel(II), Palladium (II), and Platinum(II) Complexes Having a Pyrrolyl-Iminophosphine (PNN) Pincer: Synthesis, Crystal Structures, and Cytotoxic Activity, J. Inorg. Biochem. 205 (2020) 111015, https://doi.org/10.1016/j.jinorgbio.2020.111015.

[29] C.H. Wei, Crystallographic Determination of Stereochemistry for the Triclinic and Tetragonal Modifications of a Bis-Bidentate Metal Complex, Bis(N-Tert-Butylpyrrole-2-Carbaldimino)Copper(II), Inorg. Chem. 11 (1972) 2315–2321, https://doi.org/10.1021/ic50116a005.

[30] N.A. Bailey, A. Barrass, D.E. Fenton, M.S.L. Gonzalez, R. Moody, C.O.R. De Barbarin, Compartmental Ligands. Part 10. Syntheses and Crystal and Molecular Structures of the Copper(II) Complexes of Schiff Bases Derived from 1-(Pyrrol-2-Yl)Butane-1,3-Dione and 1,3-Bis-(2-Aminophenoxy)Propane, and from Pyrrole-2-Carbaldehyde and 3,6-Dioxaoctane-1,8-Diamine, J. Chem. Soc., Dalton Trans. (1984) 2741, https://doi.org/10.1039/dt9840002741.

[31] F.Z.C. Fellah, J.-P. Costes, F. Dahan, C. Duhayon, G. Novitchi, J.-P. Tuchagues, L. Vendier, Di- and Triheteronuclear Cu−Gd and Cu−Gd−Cu Complexes with Dissymmetric Double Bridge, Inorg. Chem. 47 (2008) 6444–6451, https://doi.org/10.1021/ic800599r.

[32] Y. Hu, Q. Li, H. Li, Q. Guo, Y. Lu, Z. Li, A Novel Class of Cd(Ii), Hg(Ii) Turn-on and Cu(Ii), Zn(Ii) Turn-off Schiff Base Fluorescent Probes, Dalton Trans. 39 (2010) 11344, https://doi.org/10.1039/c0dt00737d.

[33] H. Adams, M.R.J. Elsegood, D.E. Fenton, S.L. Heath, S.J. Ryan, Dinuclear Silver(I) Complexes of Bibracchial Tetraimine Schiff Base Macrocycles Derived from Pyrrole-2,5-Dicarbaldehyde, J. Chem. Soc. Dalton Trans. (1999) 2031–2038, https://doi.org/10.1039/a901992h.

[34] K.J. Akerman, A.M. Fagenson, V. Cyril, M. Taylor, M.T. Muller, M.P. Akerman, O. Q. Munro, Gold(III) Macrocycles: Nucleotide-Specific Unconventional Catalytic Inhibitors of Human Topoisomerase I, J. Am. Chem. Soc. 136 (2014) 5670–5682, https://doi.org/10.1021/ja412350f.

[35] S. Thakur, A. Jaryal, A. Bhalla, Recent Advances in Biological and Medicinal Profile of Schiff Bases and Their Metal Complexes: An Updated Version (2018–2023), Results Chem. 7 (2024) 101350, https://doi.org/10.1016/j.rechem.2024.101350.

[36] M. Azam, S.I. Al-Resayes, A. Trzesowska-Kruszynska, R. Kruszynski, F. Shakeel, S. M. Soliman, M. Alam, M.R. Khan, S.M. Wabaidur, Zn(II) Complex Derived from Bidentate Schiff Base Ligand: Synthesis, Characterization, DFT Studies and Evaluation of Anti-Inflammatory Activity, J. Mol. Struct. 1201 (2020) 127177, https://doi.org/10.1016/j.molstruc.2019.127177.

[37] E. Pahontu, V. Fala, A. Gulea, D. Poirier, V. Tapcov, T. Rosu, Synthesis and Characterization of Some New Cu(II), Ni(II) and Zn(II) Complexes with Salicylidene Thiosemicarbazones: Antibacterial, Antifungal and in Vitro Antileukemia Activity, Molecules 18 (2013) 8812–8836, https://doi.org/10.3390/molecules18088812.

[38] R. Joshi, A. Kumari, K. Singh, H. Mishra, S. Pokharia, Triorganotin(IV) Complexes of Schiff Base Derived from 1,2,4-Triazole Moiety: Synthesis, Spectroscopic Investigation, DFT Studies, Antifungal Activity and Molecular Docking Studies, J. Mol. Struct. 1206 (2020) 127639, https://doi.org/10.1016/j.molstruc.2019.127639.

[39] S. Kaushik, S.K. Paliwal, M.R. Iyer, V.M. Patil, Promising Schiff Bases in Antiviral Drug Design and Discovery, Med. Chem. Res. 32 (2023) 1063–1076, https://doi.org/10.1007/s00044-023-03068-0.

[40] K. Buldurun, N. Turan, E. Bursal, A. Mantarcı, F. Turkan, P. Taslimi, İ. Gülçin, Synthesis, Spectroscopic Properties, Crystal Structures, Antioxidant Activities and Enzyme Inhibition Determination of Co(II) and Fe(II) Complexes of Schiff Base, Res. Chem. Intermed. 46 (2020) 283–297, https://doi.org/10.1007/s11164-019-03949-3.

[41] S. Savir, Z.J. Wei, J.W.K. Liew, I. Vythilingam, Y.A.L. Lim, H.M. Saad, K.S. Sim, K. W.Synthesis Tan, Cytotoxicity and Antimalarial Activities of Thiosemicarbazones and Their Nickel (II) Complexes, J. Mol. Struct. 1211 (2020) 128090, https://doi.org/10.1016/j.molstruc.2020.128090.

[42] M. Szymańska, I. Pospieszna-Markiewicz, M. Mańka, M. Insińska-Rak, G. Dutkiewicz, V. Patroniak, M.A. Fik-Jaskółka, Synthesis and Spectroscopic Investigations of Schiff Base Ligand and Its Bimetallic Ag(I) Complex as DNA and BSA Binders, Biomolecules 11 (2021) 1449, https://doi.org/10.3390/biom11101449.

[43] C. Liu, X. Liu, X. Ge, Q. Wang, L. Zhang, W. Shang, Y. Zhang, X.A. Yuan, L. Tian, Z. Liu, et al., Fluorescent Iridium(III) Coumarin-Salicylaldehyde Schiff Base Compounds as Lysosome-Targeted Antitumor Agents, Dalton Trans. 49 (2020) 5988–5998, https://doi.org/10.1039/D0DT00627K.

[44] M. Naqi Ahamad, K. Iman, M.K. Raza, M. Kumar, A. Ansari, M. Ahmad, M. Shahid, Anticancer Properties, Apoptosis and Catecholase Mimic Activities of Dinuclear Cobalt(II) and Copper(II) Schiff Base Complexes, Bioorg. Chem. 95 (2020) 103561, https://doi.org/10.1016/j.bioorg.2019.103561.

[45] T.J. Carneiro, A.S. Martins, M.P.M. Marques, A.M. Gil, Metabolic Aspects of Palladium(II) Potential Anti-Cancer Drugs, Front. Oncol. 10 (2020) 590970, https://doi.org/10.3389/fonc.2020.590970.

[46] F.M. Muggia, A. Bonetti, J.D. Hoeschele, M. Rozencweig, S.B. Howell, Platinum Antitumor Complexes: 50 Years Since Barnett Rosenberg's Discovery, JCO 33 (2015) 4219–4226, https://doi.org/10.1200/JCO.2015.60.7481.

[47] C.X. Zhang, S.J. Lippard, New Metal Complexes as Potential Therapeutics, Curr. Opin. Chem. Biol. 7 (2003) 481–489, https://doi.org/10.1016/S1367-5931(03)00081-4.

[48] S.N. Mbugua, N.R.S. Sibuyi, L.W. Njenga, R.A. Odhiambo, S.O. Wandiga, M. Meyer, R.A. Lalancette, M.O Onani, New Palladium(II) and Platinum(II) Complexes Based on Pyrrole Schiff Bases: Synthesis, Characterization, X-Ray Structure, and Anticancer Activity, ACS Omega 5 (2020) 14942–14954, https://doi.org/10.1021/acsomega.0c00360.

[49] T. Sen, P. Sarkar, S. Sutradhar, D. Das, B.N. Ghosh, A Review on Platinum (II/IV) Complexes of Schiff Base Ligands and Application in Biological Activity, Inorg. Chem. Commun. (2024) 113438, https://doi.org/10.1016/j.inoche.2024.113438.

[50] M. Ulular, N. Sarı, F. Han, H. Öğütcü, Hasanoğlu Özkan, E. Synthesis, Antimicrobial, and DNA-Binding Evaluation of Novel Schiff Bases Containing Tetrazole Moiety And Their Ni(II) and Pt(II) Complexes, Pharm. Chem. J. 57 (2024) 1609–1620, https://doi.org/10.1007/s11094-024-03056-7.

[51] S. Wongsuwan, J. Chatwichien, W. Sirisaksoontorn, K. Chainok, A. Songsasen, R. Chotima, Novel Pd(II) Pincer Complexes Bearing Salicylaldimine-Based Benzothiazole Derivatives: Synthesis, Structural Characterization, DNA/BSA Binding, and Biological Evaluation, New J. Chem. 47 (2023) 10624–10637, https://doi.org/10.1039/D3NJ00458A.

[52] Alam, M.N.; Almoyad, M.A.A.; Yu, J.Q.; Beale, P.; Proschogo, N.; Rupon, F.A.; Shahriar, M.; Huq, F. [Bis(Quinoline)Palladium (II) Chloride] as an Anticancer Drug Demonstrates Promising Activity on Its Own and in the Presence of 6-Shogaol 2023.

[53] R. Czarnomysy, D. Radomska, O.K. Szewczyk, P. Roszczenko, K. Bielawski, Platinum and Palladium Complexes as Promising Sources for Antitumor Treatments, IJMS 22 (2021) 8271, https://doi.org/10.3390/ijms22158271.

[54] L.E. Sarto, W.P.D. Badaró, E.P. De Gois, M.I.F. Barbosa, C. Torres, R.B. Viana, J. Honorato, E.E. Castellano, E.T. De Almeida, Crystal Structures and DFT Analysis of Palladium(II) Complexes with Schiff Bases Derived from N,N-Dialkyl-p-Phenylenediamines, J. Mol. Struct. 1204 (2020) 127549, https://doi.org/10.1016/j.molstruc.2019.127549.

[55] A.M. Abu-Dief, M.A. Said, O. Elhady, N. Alahmadi, S. Alzahrani, T.N.A. Eskander, M.A.E.A.A. Ali, Designing of Some Novel Pd (II), Ni (II) and Fe (III) Complexes: Synthesis, Structural Elucidation, Biomedical Applications, DFT and Docking Approaches against Covid-19, Inorg. Chem. Commun. 155 (2023) 110955.

[56] A.M. Abu-Dief, L.H. Abdel-Rahman, A.A.H. Abdel-Mawgoud, A Robust *in Vitro* Anticancer, Antioxidant and Antimicrobial Agents Based on New Metal-Azomethine Chelates Incorporating Ag(I), Pd (II) and VO (II) Cations: Probing the Aspects of DNA Interaction, Appl. Organomet. Chem. 34 (2020) e5373, https://doi.org/10.1002/aoc.5373.

[57] L.H. Abdel-Rahman, A.M. Abu-Dief, M.R. Shehata, F.M. Atlam, A.A.H. Abdel-Mawgoud, Some New Ag(I), VO(II) and Pd(II) Chelates Incorporating Tridentate Imine Ligand: Design, Synthesis, Structure Elucidation, Density Functional Theory Calculations for DNA Interaction, Antimicrobial and Anticancer Activities and Molecular Docking Studies, Appl. Organomet. Chem. 33 (2019) e4699, https://doi.org/10.1002/aoc.4699.

[58] S. Curry, Lessons from the Crystallographic Analysis of Small Molecule Binding to Human Serum Albumin, Drug Metab. Pharmacokinet. 24 (2009) 342–357, https://doi.org/10.2133/dmpk.24.342.

[59] A. Merlino, Metallodrug Binding to Serum Albumin: Lessons from Biophysical and Structural Studies, Coord. Chem. Rev. 480 (2023) 215026, https://doi.org/10.1016/j.ccr.2023.215026.

[60] G. De Simone, A. Di Masi, P. Ascenzi, Serum Albumin: A Multifaced Enzyme, IJMS 22 (2021) 10086, https://doi.org/10.3390/ijms221810086.

[61] X.M. He, D.C. Carter, Atomic Structure and Chemistry of Human Serum Albumin, Nature 358 (1992) 209–215, https://doi.org/10.1038/358209a0.

[62] P.A. Zunszain, J. Ghuman, T. Komatsu, E. Tsuchida, S. Curry, Crystal Structural Analysis of Human Serum Albumin Complexed with Hemin and Fatty Acid, BMC Struct. Biol. 3 (2003) 6, https://doi.org/10.1186/1472-6807-3-6.

[63] G. Rabbani, S.N.Structure Ahn, Enzymatic Activities, Glycation and Therapeutic Potential of Human Serum Albumin: A Natural Cargo, Int. J. Biol. Macromol. 123 (2019) 979–990, https://doi.org/10.1016/j.ijbiomac.2018.11.053.

[64] G. Sudlow, D.J. Birkett, D.N. Wade, The Characterization of Two Specific Drug Binding Sites on Human Serum Albumin, Mol. Pharmacol. 11 (1975) 824–832.

[65] G. Sudlow, D.J. Birkett, D.N. Wade, Further Characterization of Specific Drug Binding Sites on Human Serum Albumin, Mol. Pharmacol. 12 (1976) 1052–1061.

[66] V.T.G. Chuang, U. Kragh-Hansen, M. Otagiri, Pharmaceutical Strategies Utilizing Recombinant Human Serum Albumin, Pharm. Res. 19 (2002) 569–577, https://doi.org/10.1023/a:1015396825274.

[67] C.R. Park, M.G. Song, J.-Y. Park, H. Youn, J.-K. Chung, J.M. Jeong, Y.-S. Lee, G. J. Cheon, K.W. Kang, Conjugation of Arginylglycylaspartic Acid to Human Serum Albumin Decreases the Tumor-Targeting Effect of Albumin by Hindering Its Secreted Protein Acidic and Rich in Cysteine-Mediated Accumulation in Tumors, Am. J. Transl. Res. 12 (2020) 2488–2498.

[68] J. Wasko, M. Wolszczak, Z. Kaminski, M. Steblecka, B. Kolesinska, Human Serum Albumin Binds Native Insulin and Aggregable Insulin Fragments and Inhibits Their Aggregation, Biomolecules 10 (2020) 1366, https://doi.org/10.3390/biom10101366.

[69] H. Tao, R. Wang, W. Sheng, Y. Zhen, The Development of Human Serum Albumin-Based Drugs and Relevant Fusion Proteins for Cancer Therapy, Int. J. Biol. Macromol. 187 (2021) 24–34, https://doi.org/10.1016/j.ijbiomac.2021.07.080.

[70] M.R. Green, G.M. Manikhas, S. Orlov, B. Afanasyev, A.M. Makhson, P. Bhar, M.J. Abraxane® Hawkins, a Novel Cremophor®-Free, Albumin-Bound Particle Form of Paclitaxel for the Treatment of Advanced Non-Small-Cell Lung Cancer, Ann. Oncol. 17 (2006) 1263–1268, https://doi.org/10.1093/annonc/mdl104.

[71] N. Desai, Nanoparticle Albumin-Bound Paclitaxel (Abraxane®), in: M. Otagiri, V. T.G. Chuang (Eds.), Albumin in Medicine, Springer Singapore, Singapore, 2016, pp. 101–119. ISBN 978-981-10-2115-2.

[72] H. Cho, S.I. Jeon, C.-H. Ahn, M.K. Shim, K. Kim, Emerging Albumin-Binding Anticancer Drugs for Tumor-Targeted Drug Delivery: Current Understandings and Clinical Translation, Pharmaceutics 14 (2022) 728, https://doi.org/10.3390/pharmaceutics14040728.

[73] S. Sookai, O. Q Munro, Spectroscopic and Computational Study of the Interaction of Pt(Ii) Pyrrole-Imine Chelates with Human Serum Albumin, Dalton Trans. 52 (2023) 14774–14789, https://doi.org/10.1039/D3DT02039H.

[74] O.Q. Munro, G.L. Camp, Self-Recognition in a Flexible Bis(Pyrrole) Schiff Base Derivative: Formation of a One-Dimensional Hydrogen-Bonded Polymer, Acta Crystallogr. C 59 (2003) o672–o675, https://doi.org/10.1107/S0108270103023230.

[75] O.Q. Munro, S.D. Joubert, C.D. Grimmer, Molecular Recognition: Preorganization of a Bis(Pyrrole) Schiff Base Derivative for Tight Dimerization by Hydrogen Bonding, Chem. Eur. J. 12 (2006) 7987–7999, https://doi.org/10.1002/chem.200600403.

[76] M.P. Akerman, T. Chatturgoon, O.Q. Munro, An X-Ray Crystallographic and DFT Study of Bis(Pyrrolide-Imine) Nickel(II) Schiff Base Chelates, Inorg. Chim. Acta 421 (2014) 292–299, https://doi.org/10.1016/j.ica.2014.06.015.

[77] A. Datta, N.K. Karan, S. Mitra, V. Gramlich, Synthesis and Structural Characterization of a (N,N′-Bis[2(S)-Pyrrolidylmethyl]-Propane-1,3-Diamine) Nickel (II) Complex, J. Chem. Crystallogr. 33 (2003) 579–583, https://doi.org/10.1023/A:1024299005045.

[78] S. Sookai, O.Q. Munro, Complexities of the Interaction of NiII, PdII and PtII Pyrrole-Imine Chelates with Human Serum Albumin**, ChemistryEurope 1 (2023) e202300012, https://doi.org/10.1002/ceur.202300012.

[79] D. van der Westhuizen, D. I Bezuidenhout, O. Q Munro, Cancer Molecular Biology and Strategies for the Design of Cytotoxic Gold(i) and Gold(Iii) Complexes: A Tutorial Review, Dalton Trans. 50 (2021) 17413–17437, https://doi.org/10.1039/D1DT02783B.

[80] E. Alessio, Thirty Years of the Drug Candidate NAMI-A and the Myths in the Field of Ruthenium Anticancer Compounds: A Personal Perspective, Dalton Transactions 2017 (2017) 1549–1560, https://doi.org/10.1002/ejic.201600986.

[81] T.P. Jr, All About Albumin: Biochemistry, Genetics, and Medical Applications, Academic Press, 1995. ISBN 978-0-08-052704-8.

[82] N. Myeza, C. Slabber, O.Q. Munro, S. Sookai, S.C. Zacharias, C. Martins-Furness, L. Harmse, An 8-Aminoquinoline-Naphthyl Copper Complex Causes Apoptotic Cell Death by Modulating the Expression of Apoptotic Regulatory Proteins in Breast Cancer Cells, Eur. J. Pharmacol. 978 (2024) 176764, https://doi.org/10.1016/j.ejphar.2024.176764.

[83] S. Keller, Y.C. Ong, Y. Lin, K. Cariou, G. Gasser, A Tutorial for the Assessment of the Stability of Organometallic Complexes in Biological Media, J. Organomet. Chem. 906 (2020) 121059.
[84] E. Brouwer, J. Verweij, P. De Bruijn, W.J. Loos, M. Pillay, D. Buijs, A. Sparreboom, Measurement of Fraction Unbound Paclitaxel in Human Plasma, Drug Metab. Dispos. 28 (2000) 1141–1145.
[85] S. Sookai, S. Perumal, M. Kaur, O.Q. Munro, Pt (II) Bis (Pyrrole-Imine) Complexes: Luminescent Probes and Cytotoxicity in MCF-7 Cells, J. Inor. Biochem. (2024) 112617.
[86] Ö. Altun, M.Ö. Koçer, Pt (II) Complex of Schiff Base Derived from L-Phenylalanine and Furfuraldehyde in the Presence of 8-Hydroxyquinoline: Structural Analysis, Composition of Complex and Biological Activity, C. R. Chim. 23 (2020) 127–142.
[87] S. Kouser, M. Joythi, A.B. Begum, M.S. Asha, F.H. Al-Ostoot, D.P. Lakshmeesha, R. Ramu, S.A. Khanum, Molecular Docking, Synthesis and Antimicrobial Evaluation of Metal Complexes with Schiff Base, Results Chem. 5 (2023) 100650.
[88] P. Nithya, R. Rajamanikandan, J. Simpson, M. Ilanchelian, S. Govindarajan, Solvent Assisted Synthesis, Structural Characterization and Biological Evaluation of Cobalt (II) and Nickel (II) Complexes of Schiff Bases Generated from Benzyl Carbazate and Cyclic Ketones, Polyhedron 145 (2018) 200–217.
[89] S. Sookai, M. Akerman, M. Færch, Y. Sayed, O.Q. Munro, Cytotoxic Pyrrole-Based Gold (III) Chelates Target Human Topoisomerase II as Dual-Mode Inhibitors and Interact with Human Serum Albumin, Eur. J. Med. Chem. (2025) 117330.
[90] S. Goutelle, M. Maurin, F. Rougier, X. Barbaut, L. Bourguignon, M. Ducher, P. Maire, The Hill Equation: A Review of Its Capabilities in Pharmacological Modelling, Fundam. Clin. Pharmacol. 22 (2008) 633–648.
[91] B.H. Geierstanger, D.E. Wemmer, Complexes of the Minor Groove of DNA, Annu. Rev. Biophys. Biomol. Struct. 24 (1995) 463–493.
[92] P.E. Pjura, K. Grzeskowiak, R.E. Dickerson, Binding of Hoechst 33258 to the Minor Groove of B-DNA, J. Mol. Biol. 197 (1987) 257–271.
[93] K.M. Prabhu Kumar, B.C. Vasantha Kumar, P.R. Kumar, R.J. Butcher, H.K. Vivek, P.A. Suchetan, H.D. Revanasiddappa, S. Foro, Synthesis, Characterization, CT-DNA Binding and Docking Studies of Novel Selenated Ligands and Their Palladium Complexes, Appl. Organomet. Chem. 34 (2020) e5634, https://doi.org/10.1002/aoc.5634.
[94] C.V. Barra, F.V. Rocha, L. Morel, A. Gautier, S.S. Garrido, A.E. Mauro, R.C. Frem, A.V. Netto, DNA Binding, Topoisomerase Inhibition and Cytotoxicity of Palladium (II) Complexes with 1, 10-Phenanthroline and Thioureas, Inorg. Chim. Acta 446 (2016) 54–60.
[95] S. Kemp, N.J. Wheate, D.P. Buck, M. Nikac, J.G. Collins, J.R. Aldrich-Wright, The Effect of Ancillary Ligand Chirality and Phenanthroline Functional Group Substitution on the Cytotoxicity of Platinum (II)-Based Metallointercalators, J. Inorg. Biochem. 101 (2007) 1049–1058.
[96] M. Vorlícková, Conformational Transitions of Alternating Purine-Pyrimidine DNAs in Perchlorate Ethanol Solutions, Biophys. J. 69 (1995) 2033–2043.
[97] J. Kypr, M. Vorlícková, Circular Dichroism Spectroscopy Reveals Invariant Conformation of Guanine Runs in DNA, Biopolym. Orig. Res. Biomol. 67 (2002) 275–277.
[98] M. Vorlícková, I. Kejnovská, J. Kovanda, J. Kypr, Conformational Properties of DNA Strands Containing Guanine-Adenine and Thymine-Adenine Repeats, Nucleic Acids Res. 26 (1998) 1509–1514.
[99] E. Froehlich, J.S. Mandeville, C.M. Weinert, L. Kreplak, H.A. Tajmir-Riahi, Bundling and Aggregation of DNA by Cationic Dendrimers, Biomacromolecules 12 (2011) 511–517.
[100] L. Rosenfeld, Quantenmechanische Theorie der natürlichen optischen Aktivität von Flüssigkeiten und Gasen, Z. Phys. 52 (1929) 161–174, https://doi.org/10.1007/BF01342393.
[101] S. Sookai, M.L. Bracken, M. Nowakowska, Spectroscopic and Computational pH Study of NiII and PdII Pyrrole-Imine Chelates with Human Serum Albumin, Molecules 28 (2023) 7466.
[102] S. Allenmark, Induced Circular Dichroism by Chiral Molecular Interaction, Chirality 15 (2003) 409–422, https://doi.org/10.1002/chir.10220.
[103] G. Gottarelli, S. Lena, S. Masiero, S. Pieraccini, G.P. Spada, The Use of Circular Dichroism Spectroscopy for Studying the Chiral Molecular Self-Assembly: An Overview, Chirality 20 (2008) 471–485, https://doi.org/10.1002/chir.20459.
[104] B. Nordén, T. Kurucsev, Analysing DNA Complexes by Circular and Linear Dichroism, J. Mol. Recognit. 7 (1994) 141–155.
[105] Y. Kubota, K. Hashimoto, K. Fujita, M. Wakita, E. Miyanohana, Y. Fujisaki, Flow Dichroism, Flow Polarized Fluorescence and Viscosity of the DNA · Acridine Complexes, Biochim. Biophys. Acta (BBA) Nucleic Acids Protein Synth. 478 (1977) 23–32, https://doi.org/10.1016/0005-2787(77)90240-4.
[106] P.C. Dedon, Determination of Binding Mode: Intercalation, Curr. Protoc. Nucleic Acid Chem. 00 (2000), https://doi.org/10.1002/0471142700.nc0801s00, 8.1.1-8.1.13.
[107] M.A. Galindo, D. Olea, M.A. Romero, J. Gómez, P. del Castillo, M.J. Hannon, A. Rodger, F. Zamora, J.A.R. Navarro, Design and Non-Covalent DNA Binding of Platinum(II) Metallacalix[4]Arenes, Chem. Eur. J. 13 (2007) 5075–5081, https://doi.org/10.1002/chem.200601581.
[108] H. Rozenberg, D. Rabinovich, F. Frolow, R.S. Hegde, Z. Shakked, Structural Code for DNA Recognition Revealed in Crystal Structures of Papillomavirus E2-DNA Targets, Proc. Natl. Acad. Sci. USA 95 (1998) 15194–15199, https://doi.org/10.1073/pnas.95.26.15194.
[109] H. Song, J.T. Kaiser, J.K. Barton, Crystal Structure of Δ-[Ru (Bpy) 2 Dppz] 2+ Bound to Mismatched DNA Reveals Side-by-Side Metalloinsertion and Intercalation, Nat. Chem. 4 (2012) 615–620.
[110] A.R. Leach, B.K. Shoichet, C.E. Peishoff, Prediction of Protein−Ligand Interactions. Docking and Scoring: Successes and Gaps, J. Med. Chem. 49 (2006) 5851–5855, https://doi.org/10.1021/jm060999m.
[111] G.L. Warren, C.W. Andrews, A.-M. Capelli, B. Clarke, J. LaLonde, M.H. Lambert, M. Lindvall, N. Nevins, S.F. Semus, S. Senger, et al., A Critical Assessment of Docking Programs and Scoring Functions, J. Med. Chem. 49 (2006) 5912–5931, https://doi.org/10.1021/jm050362n.
[112] K.J. Akerman, A.M. Fagenson, V. Cyril, M. Taylor, M.T. Muller, M.P. Akerman, O. Q. Munro, Gold(III) Macrocycles: Nucleotide-Specific Unconventional Catalytic Inhibitors of Human Topoisomerase I, J. Am. Chem. Soc. 136 (2014) 5670–5682, https://doi.org/10.1021/ja412350f.
[113] M.P. O'Hagan, S. Haldar, J.C. Morales, A.J. Mulholland, M.C. Galan, Enhanced Sampling Molecular Dynamics Simulations Correctly Predict the Diverse Activities of a Series of Stiff-Stilbene G-Quadruplex DNA Ligands, Chemical Science 12 (2021) 1415–1426.
[114] J. Costa Pessoa, I. Tomaz, Transport of Therapeutic Vanadium and Ruthenium Complexes by Blood Plasma Components, Curr. Med. Chem. 17 (2010) 3701–3738.
[115] G. Rabbani, S.N. Ahn, Structure, Enzymatic Activities, Glycation and Therapeutic Potential of Human Serum Albumin: A Natural Cargo, Int. J. Biol. Macromol. 123 (2019) 979–990, https://doi.org/10.1016/j.ijbiomac.2018.11.053.
[116] O.K. Abou-Zied, O.I.K. Al-Shihi, Characterization of Subdomain IIA Binding Site of Human Serum Albumin in Its Native, Unfolded, and Refolded States Using Small Molecular Probes, J. Am. Chem. Soc. 130 (2008) 10793–10801, https://doi.org/10.1021/ja8031289.
[117] P.R. Callis, Binding Phenomena and Fluorescence Quenching. II: Photophysics of Aromatic Residues and Dependence of Fluorescence Spectra on Protein Conformation, J. Mol. Struct. 1077 (2014) 22–29, https://doi.org/10.1016/j.molstruc.2014.04.051.
[118] Y. Yue, J. Liu, M. Yao, X. Yao, J. Fan, H. Ji, The Investigation of the Binding Behavior between Ethyl Maltol and Human Serum Albumin by Multi-Spectroscopic Methods and Molecular Docking, Spectrochimica Acta Part A: Molecular and Biomolecular Spectroscopy 96 (2012) 316–323, https://doi.org/10.1016/j.saa.2012.05.041.
[119] A.M. Abu-Dief, R.M. El-Khatib, F.S. Aljohani, S.O. Alzahrani, A. Mahran, M. E. Khalifa, N.M. El-Metwaly, Synthesis and Intensive Characterization for Novel Zn (II), Pd (II), Cr (III) and VO (II)-Schiff Base Complexes; DNA-Interaction, DFT, Drug-Likeness and Molecular Docking Studies, J. Mol. Struct. 1242 (2021) 130693.
[120] A.M. Abu-Dief, H.M. El-Sagher, M.R. Shehata, Fabrication, Spectroscopic Characterization, Calf Thymus DNA Binding Investigation, Antioxidant and Anticancer Activities of Some Antibiotic Azomethine Cu(II), Pd(II), Zn(II) and Cr (III) Complexes, Appl. Organomet. Chem. 33 (2019) e4943, https://doi.org/10.1002/aoc.4943.
[121] M.H. Gehlen, The Centenary of the Stern-Volmer Equation of Fluorescence Quenching: From the Single Line Plot to the SV Quenching Map, J. Photochem. Photobiol. C Photochem. Rev. 42 (2020) 100338, https://doi.org/10.1016/j.jphotochemrev.2019.100338.
[122] K. Flora, J.D. Brennan, G.A. Baker, M.A. Doody, F.V. Bright, Unfolding of Acrylodan-Labeled Human Serum Albumin Probed by Steady-State and Time-Resolved Fluorescence Methods, Biophys. J. 75 (1998) 1084–1096, https://doi.org/10.1016/S0006-3495(98)77598-8.
[123] M.K. Helms, C.E. Petersen, N.V. Bhagavan, D.M. Jameson, Time-Resolved Fluorescence Studies on Site-Directed Mutants of Human Serum Albumin, FEBS Letters 408 (1997) 67–70, https://doi.org/10.1016/S0014-5793(97)00389-X.
[124] O.K. Abou-Zied, O.I.K. Al-Shihi, Characterization of Subdomain IIA Binding Site of Human Serum Albumin in Its Native, Unfolded, and Refolded States Using Small Molecular Probes, J. Am. Chem. Soc. 130 (2008) 10793–10801, https://doi.org/10.1021/ja8031289.
[125] Y.-J. Hu, Y. Liu, X.-H. Xiao, Investigation of the Interaction between Berberine and Human Serum Albumin, Biomacromolecules 10 (2009) 517–521, https://doi.org/10.1021/bm801120k.
[126] G.G. Ariga, P.N. Naik, S.A. Chimatadar, S.T. Nandibewoor, Interactions between Epinastine and Human Serum Albumin: Investigation by Fluorescence, UV–Vis, FT–IR, CD, Lifetime Measurement and Molecular Docking, J. Mol. Struct. 1137 (2017) 485–494, https://doi.org/10.1016/j.molstruc.2016.12.066.
[127] X. Sun, S. Bi, J. Wu, R. Zhao, D. Shao, Z. Song, Multispectral and Molecular Docking Investigations on the Interaction of Primethamine/Trimethoprim with BSA/HSA, J. Biomol. Struct. Dyn. 38 (2020) 934–942, https://doi.org/10.1080/07391102.2019.1588785.
[128] C.-M. Che, S.-C. Chan, H.-F. Xiang, M.C.W. Chan, Y. Liu, Y. Wang, Tetradentate Schiff Base Platinum(II) Complexes as New Class of Phosphorescent Materials for High-Efficiency and White-Light Electroluminescent Devices, Chem. Commun. (2004) 1484–1485, https://doi.org/10.1039/B402318H.
[129] P.D. Ross, S. Subramanian, Thermodynamics of Protein Association Reactions: Forces Contributing to Stability, Biochemistry 20 (1981) 3096–3102, https://doi.org/10.1021/bi00514a017.
[130] X. Li, S. Wang, Study on the Interaction of (+)-Catechin with Human Serum Albumin Using Isothermal Titration Calorimetry and Spectroscopic Techniques, New J. Chem. 39 (2015) 386–395, https://doi.org/10.1039/C4NJ01344A.
[131] P.D. Ross, S. Subramanian, Thermodynamics of Protein Association Reactions: Forces Contributing to Stability, Biochemistry 20 (1981) 3096–3102, https://doi.org/10.1021/bi00514a017.
[132] X.M. He, D.C. Carter, Atomic Structure and Chemistry of Human Serum Albumin, Nature 358 (1992) 209–215, https://doi.org/10.1038/358209a0.

[133] S. Sookai, M. P Akerman, O. Q Munro, Chiral Au(Iii) Chelates Exhibit Unique NCI-60 Cytotoxicity Profiles and Interactions with Human Serum Albumin, Dalton Trans. 53 (2024) 5089–5104, https://doi.org/10.1039/D3DT04024K.
[134] P.W. Ayers, The Physical Basis of the Hard/Soft Acid/Base Principle, Faraday Discuss 135 (2006) 161–190, https://doi.org/10.1039/B606877D.
[135] R.G. Pearson, Hard and Soft Acids and Bases, HSAB, Part II: Underlying Theories, J. Chem. Educ. 45 (1968) 643, https://doi.org/10.1021/ed045p643.
[136] M. Kolář, T. Kubař, P. Hobza, On the Role of London Dispersion Forces in Biomolecular Structure Determination, J. Phys. Chem. B 115 (2011) 8038–8046, https://doi.org/10.1021/jp202878d.
[137] R.E. Olson, D.D. Christ, Chapter 33. Plasma Protein Binding of Drugs, in: J. A. Bristol (Ed.), Annual Reports in Medicinal Chemistry 31, Academic Press, 1996, pp. 327–336.
[138] H. Aki, M. Goto, M. Yamamoto, Thermodynamic Aspects of the Molecular Recognition of Drugs by Human Serum Albumin, Thermochim. Acta 251 (1995) 379–388, https://doi.org/10.1016/0040-6031(94)02053-Q.
[139] H. Aki, M. Yamamoto, Thermodynamics of the Binding of Phenothiazines to Human Plasma, Human Serum Albumin and A1-Acid Glycoprotein: A Calorimetric Study, J. Pharm. Pharmacol. 41 (1989) 674–679, https://doi.org/10.1111/j.2042-7158.1989.tb06339.x.
[140] H. Aki, M. Yamamoto, Thermodynamic characterization of drug binding to human serum albumin by isothermal titration microcalorimetry, J. Pharm. Sci. 83 (1994) 1712–1716, https://doi.org/10.1002/jps.2600831213.
[141] I. Petitpas, A.A. Bhattacharya, S. Twine, M. East, S. Curry, Crystal Structure Analysis of Warfarin Binding to Human Serum Albumin: ANATOMY OF DRUG SITE I *, J. Biol. Chem. 276 (2001) 22804–22809, https://doi.org/10.1074/jbc.M100575200.
[142] M.J. Moreno, L.M.S. Loura, J. Martins, A. Salvador, A. Velazquez-Campoy, Analysis of the Equilibrium Distribution of Ligands in Heterogeneous Media-Approaches and Pitfalls, Int. J. Mol. Sci. 23 (2022) 9757, https://doi.org/10.3390/ijms23179757.
[143] S.M. Kelly, T.J. Jess, N.C. Price, How to Study Proteins by Circular Dichroism, Biochim. Biophys. Acta (BBA) Proteins Proteom. 1751 (2005) 119–139, https://doi.org/10.1016/j.bbapap.2005.06.005.
[144] N. Sreerama, R.W. Woody, Computation and Analysis of Protein Circular Dichroism Spectra. Methods in Enzymology; Numerical Computer Methods, Part D, Academic Press, 2004, pp. 318–351. Vol. 383.
[145] A. Micsonai, F. Wien, É. Bulyáki, J. Kun, É. Moussong, Y.-H. Lee, Y. Goto, M. Réfrégiers, J. Kardos, BeStSel: A Web Server for Accurate Protein Secondary Structure Prediction and Fold Recognition from the Circular Dichroism Spectra, Nucleic Acids Res. 46 (2018) W315–W322, https://doi.org/10.1093/nar/gky497.
[146] F. Mohammadi, A.-K. Bordbar, A. Divsalar, K. Mohammadi, A.A. Saboury, Analysis of Binding Interaction of Curcumin and Diacetylcurcumin with Human and Bovine Serum Albumin Using Fluorescence and Circular Dichroism Spectroscopy, Protein J. 28 (2009) 189–196.
[147] H.A. Tajmir-Riahi, C.N. N'Soukpoe-Kossi, D. Joly, Structural Analysis of Protein–DNA and Protein–RNA Interactions by FTIR, UV-Visible and CD Spectroscopic Methods, Spectroscopy 23 (2009) 81–101.
[148] A. Khammari, A.A. Saboury, M.H. Karimi-Jafari, M. Khoobi, A. Ghasemi, S. Yousefinejad, O.K. Abou-Zied, Insights into the Molecular Interaction between Two Polyoxygenated Cinnamoylcoumarin Derivatives and Human Serum Albumin, Chem. Chem. Phys. 19 (2017) 10099–10115.
[149] P. Alam, S.K. Chaturvedi, T. Anwar, M.K. Siddiqi, M.R. Ajmal, G. Badr, M. H. Mahmoud, R. Hasan Khan, Biophysical and Molecular Docking Insight into the Interaction of Cytosine β-D Arabinofuranoside with Human Serum Albumin, J. Lumin. 164 (2015) 123–130, https://doi.org/10.1016/j.jlumin.2015.03.011.
[150] D. Lafitte, P.O. Tsvetkov, F. Devred, R. Toci, F. Barras, C. Briand, A.A. Makarov, J. Haiech, Cation Binding Mode of Fully Oxidised Calmodulin Explained by the Unfolding of the Apostate, Biophys. Acta (BBA) Proteins Proteom 1600 (2002) 105–110.
[151] O.K. Abou-Zied, O.I.K. Al-Shihi, Characterization of Subdomain IIA Binding Site of Human Serum Albumin in Its Native, Unfolded, and Refolded States Using Small Molecular Probes, J. Am. Chem. Soc. 130 (2008) 10793–10801, https://doi.org/10.1021/ja8031289.
[152] S.M. Kelly, N.C. Price, The Use of Circular Dichroism in the Investigation of Protein Structure and Function, Curr. Protein Pept. Sci. 1 (2000) 349–384.
[153] X.-X. Cheng, X.-Y. Fan, F.-L. Jiang, Y. Liu, K.-L. Lei, Resonance Energy Transfer, pH-Induced Folded States and the Molecular Interaction of Human Serum Albumin and Icariin, Luminescence 30 (2015) 1026–1033.
[154] A. Barth, S.R. Martin, P.M. Bayley, Resolution of Trp near UV CD Spectra of Calmodulin-Domain Peptide Complexes into the 1La and 1Lb Component Spectra, Biopolym. Orig. Res. Biomol. 45 (1998) 493–501.
[155] B. Valeur, G. Weber, Resolution of the Fluorescence Excitation Spectrum of Indole into the 1La and 1Lb Excitation Bands, Photochem. Photobiol. 25 (1977) 441–444.
[156] T. Vreven, K.S. Byun, I. Komáromi, S. Dapprich, J.A. Montgomery, K. Morokuma, M.J. Frisch, Combining Quantum Mechanics Methods with Molecular Mechanics Methods in ONIOM, J. Chem. Theory Comput. 2 (2006) 815–826, https://doi.org/10.1021/ct050289g.
[157] A.K. Rappe, C.J. Casewit, K.S. Colwell, W.A. Goddard, W.M. Skiff, UFF, a Full Periodic Table Force Field for Molecular Mechanics and Molecular Dynamics Simulations, J. Am. Chem. Soc. 114 (1992) 10024–10035, https://doi.org/10.1021/ja00051a040.